Translational activity of the splicing factor SRSF1 is required for development and cilia function

Fiona Haward,[1,5,6] Magdalena M. Maslon,[1,6] Patricia L. Yeyati,[1,6] Nicolas Bellora,[2] Jan N. Hansen,[3] Stuart Aitken,[1] Jennifer Lawson,[1] Alex von Kriegsheim,[4] Dagmar Wachten,[3] Pleasantine Mill,[1,*] Ian R. Adams[1,*] and Javier F. Cáceres[1,7,*]

[1]MRC Human Genetics Unit, Institute of Genetics and Molecular Medicine, University of Edinburgh, Crewe Road South, Edinburgh EH4 2XU, UK

[2]IPATEC, Consejo Nacional de Investigaciones, Científicas y Técnicas (CONICET)-Universidad Nacional del Comahue, 8400, Bariloche, Argentina.

[3]Institute of Innate Immunity, Biophysical Imaging, Medical Faculty, University of Bonn, Bonn, Germany

[4]Edinburgh Cancer Research UK Centre, Institute of Genetics and Molecular Medicine, University of Edinburgh, Crewe Road South, Edinburgh EH4 2XU, UK

[5]Present address: Centre for Gene Regulation and Expression, School of Life Sciences, University of Dundee, Dundee DD1 5EH, UK

[6]These authors contributed equally to this work

[7]Lead contact

*Correspondence: Pleasantine.Mill@igmm.ed.ac.uk; Ian.Adams@igmm.ed.ac.uk; Javier.Caceres@igmm.ed.ac.uk

Running title: Nucleo-cytoplasmic shuttling of SR proteins

[Key Words: SR proteins; SRSF1; alternative splicing; mRNA translation; cilia]

HIGHLIGHTS

- A mouse model reveals the physiological role of SRSF1 nucleo-cytoplasmic shuttling
- Restricting SRSF1 to the nucleus results in perinatal phenotypes in the mouse
- Precluding SRSF1 shuttling disrupts mRNA translation and impacts on motile cilia
- SRSF1 shuttling reprograms gene expression at the level of mRNA translation

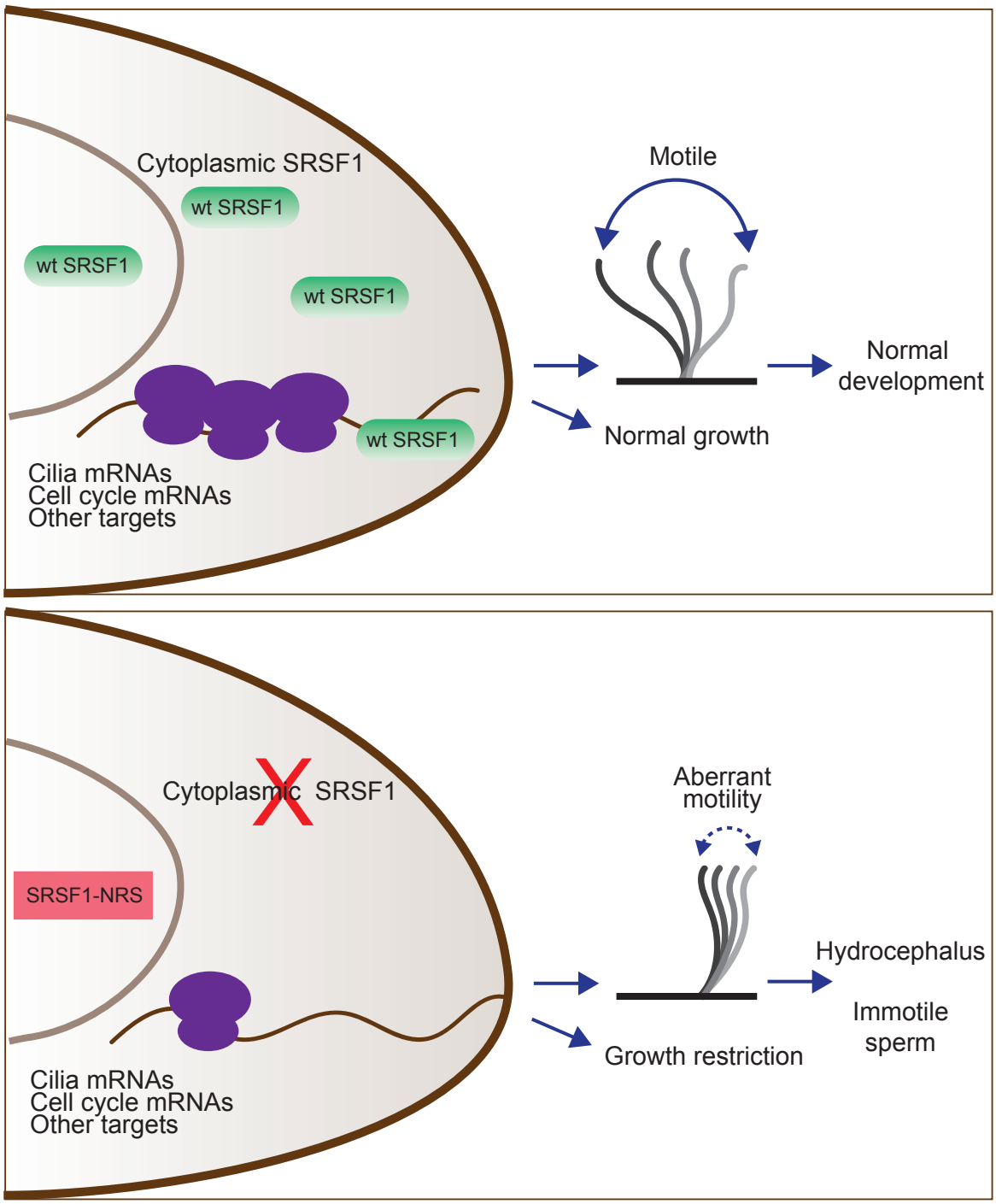
Cytoplasmic SRSF1
wt SRSF1
wt SRSF1
wt SRSF1
wt SRSF1
Cilia mRNAs
Cell cycle mRNAs
Other targets
Motile
Normal development
Normal growth
Cytoplasmic SRSF1
SRSF1-NRS
Cilia mRNAs
Cell cycle mRNAs
Other targets
Aberrant motility
Hydrocephalus
Immotile sperm
Growth restriction

SUMMARY

Shuttling RNA-binding proteins coordinate nuclear and cytoplasmic steps of gene expression. SR proteins regulate pre-mRNA splicing in the nucleus and a subset of them, including SRSF1, shuttles between the nucleus and cytoplasm affecting post-splicing processes. However, the physiological significance of this remains unclear. Here, we used genome editing to knock-in a nuclear retention signal (NRS) in *Srsf1* to create a mouse model harboring an SRSF1 protein that is retained exclusively in the nucleus. *Srsf1* $^{NRS/NRS}$ mutants displayed small body size, hydrocephalus and immotile sperm, all traits associated with ciliary defects. We observed reduced translation of a subset of mRNAs and decreased abundance of proteins involved in multiciliogenesis, with disruption of ciliary ultrastructure and motility. These results highlight the physiological requirement of splicing factor shuttling to reprogram gene expression networks at the level of mRNA translation in the context of high cellular demand for cilia function.

INTRODUCTION

Alternative splicing is an essential step in the gene expression cascade that generates a vast number of mRNA isoforms to shape the proteomes of multicellular eukaryotes (Baralle and Giudice, 2017; Ule and Blencowe, 2019). It is largely controlled by the binding of RNA-binding proteins (RBPs) in a manner dependent on the cellular context (Fu and Ares, 2014). Additional layers of regulation include alterations in chromatin state and the co-transcriptional nature of the splicing process, including the rate of RNA Polymerase II (RNAPII) elongation (Maslon et al., 2019; Naftelberg et al., 2015; Saldi et al., 2016).

The serine/arginine-rich (SR) family proteins are among the most extensively characterized regulators of pre-mRNA splicing (Wegener and Müller-McNicoll, 2019; Zhou and Fu, 2013). Their modular domain structure comprises one or two RNA recognition motifs (RRMs) at their N-termini that contribute to sequence-specific RNA-binding and a C-terminal RS domain (arginine and serine repeats) that promotes protein-protein interactions (Howard and Sanford, 2015). The RS domain also acts as a nuclear localization signal by promoting the interaction with the SR protein nuclear import receptor, transportin-SR (Cáceres et al., 1997; Kataoka et al., 1999; Lai et al., 2000). The role of SR proteins in alternative splicing regulation can be antagonized by heterogeneous nuclear ribonucleoproteins (hnRNPs). Thus, the relative ratio of these two protein families can regulate alternative splicing patterns that generate specific cell lineages and tissues during development (Busch and Hertel, 2012; Hanamura et al., 1998; Zhu et al., 2001).

Besides the clearly defined nuclear roles of SR family proteins, a subset of these, of which SRSF1 is the prototype, shuttle continuously from the nucleus to the cytoplasm and are involved in post-splicing activities (Cáceres et al., 1998; Cowper et al., 2001; Sapra et al., 2009). These include mRNA export as well as cytoplasmic roles such as mRNA translation, nonsense-mediated decay (NMD) and regulation of RNA stability (reviewed by (Long and Caceres, 2009;

Twyffels et al., 2011)). Several protein kinases phosphorylate the RS domain of SR proteins, including the SRPK family (Gui et al., 1994; Ngo et al., 2008) and the Clk/Sty family dual-specificity kinases (Prasad et al., 1999). Whereas phosphorylated SR proteins are required for spliceosome assembly, subsequent dephosphorylation is required for splicing catalysis and for sorting shuttling and non-shuttling SR proteins in the nucleus (Lin et al., 2005). Our previous work demonstrated that hypophosphorylated SRSF1 is associated with polyribosomes and promotes translation of mRNAs in an mTOR-dependent manner (Michlewski et al., 2008; Sanford et al., 2004, 2005). We subsequently showed that translational targets of SRSF1 predominantly encode proteins that localize to centrosomes and are required for cell cycle regulation and chromosome segregation (Maslon et al., 2014). The shuttling ability of individual SR proteins has also been usurped by viruses, as seen with the role of individual SR proteins in promoting translation of viral transcripts, including poliovirus, MMPV and HIV (Bedard et al., 2007; Mahiet and Swanson, 2016; Swartz et al., 2007).

SRSF1 is essential for cellular viability (Lin et al., 2005; Wang et al., 1996) and has been shown to act as an oncogene and to promote mammary epithelial cell transformation (Anczuków et al., 2012; Karni et al., 2007). In living animals, its targeted disruption results in early embryonic lethality that cannot be rescued by other SR proteins (Möröy and Heyd, 2007; Xu et al., 2005). Furthermore, a T cell-restricted *Srsf1*-deficient mice develops systemic autoimmunity and lupus-nephritis (Katsuyama et al., 2019). This evidence highlights the splicing roles of SRSF1 in cellular transformation or in the development of tissues. By contrast, the physiological relevance of their post-splicing activities has remained fully enigmatic. In particular, the splicing independent roles of SRSF1 are not understood in the context of a developing organism and lineage specification.

Here, we have engineered a mouse model of a non-shuttling endogenous SRSF1 protein that is exclusively retained in the nucleus. We have used CRISPR/Cas9 genome editing to non-

disruptively knock-in a potent nuclear retention signal (NRS) at the C-terminus of the *Srsf1* genomic locus. This sequence is naturally present in the non-shuttling SR protein SRSF2 and when fused to SRSF1 prevents its shuttling when overexpressed (Cazalla et al., 2002; Maslon et al., 2014; Sanford et al., 2004). Here, we demonstrate that precluding the shuttling ability of SRSF1 preserves its splicing function. We show that SRSF1 nucleo-cytoplasmic shuttling is dispensable for embryonic development; however, mutant animals display characteristic motile cilia phenotypes. We also observed that the lack of cytoplasmic SRSF1 leads to decreased translation of a subset of mRNAs that are required during the development of functional motile ciliated tissues. Importantly, these molecular changes are consistent with the phenotypic abnormalities found in the *Srsf1*$^{NRS/NRS}$ mice. We conclude that the translational activity of SRSF1 is indeed required for proper development and primarily affects biogenesis and function of motile cilia.

RESULTS

Generation of a non-shuttling SRSF1 protein mouse model

To create an *in vivo* model expressing only a nuclear-retained SRSF1 protein, we inserted into the endogenous mouse locus a naturally occurring nuclear retention signal (NRS), present in the exclusively nuclear related SR protein SRSF2 (Figure 1A) (Cazalla et al., 2002). We designed a CRISPR/Cas9-assisted strategy in which an NRS sequence, a small linker and a T7 tag were introduced at the C-terminus of the canonical SRSF1 isoform (Sun et al., 2010) (Figure 1B and S1). This approach minimizes perturbation of the N-terminal RRM domains of SRSF1 that are crucial for RNA recognition and its function in splicing (Cléry et al., 2013) The presence of the T7 tag facilitates both visualization of the tagged protein (referred herein as SRSF1-NRS), as well as biochemical experiments. In contrast to the completely penetrant early embryonic lethality of *Srsf1*$^{-/-}$ knockout mice (Xu et al., 2005), *Srsf1*$^{NRS/NRS}$ mice were born from *Srsf1*$^{+/NRS}$ intercrosses and survived postnatally to the point of genotyping (day 14) (Figure 1C). However, postnatal *Srsf1*$^{NRS/NRS}$ mice displayed overt phenotypic abnormalities from this stage onwards (see later). These findings indicate that the cytoplasmic functions for SRSF1 allele are mostly dispensable for embryonic development. We confirmed that the SRSF1-NRS fusion protein is expressed in liver tissue and embryonic stem cells (ESCs) derived from homozygous *Srsf1*$^{NRS/NRS}$ mice (Figure 1D).

We and others have previously shown that the SRSF1-NRS chimeric protein is retained in the nucleus (Cazalla et al., 2002; Lin et al., 2005). Here, we analyzed the shuttling ability of endogenous SRSF1-NRS protein in neural stem cells (NSCs) differentiated *in vitro* from ESCs derived from *Srsf1*$^{NRS/NRS}$ animals, using an inter-species heterokaryon assay (Piñol-Roma and Dreyfuss, 1992). As expected, we observed that SRSF1-NRS protein was only detected in the mouse but not in human nuclei, confirming that it is indeed restricted to the mouse nucleus (Figure S2, lower panel). As a positive control, we transiently expressed a T7-tagged WT-

SRSF1 in mouse NSCs and clearly observed its presence in the recipient HeLa nuclei, underlining the innate shuttling activity of WT SRSF1 (Figure S2, upper panel). This confirms that our targeting strategy was successful and the resulting SRSF1-NRS fusion protein expressed from the endogenous *Srsf1* locus is in fact restricted to the nucleus.

Srsf1$^{NRS/NRS}$ mice are growth restricted

The viability of *Srsf1*$^{NRS/NRS}$ embryos contrasts with the reported lethality of *Srsf1* null embryos by E7.5 (Xu et al., 2005). Strikingly, homozygous *Srsf1*$^{NRS/NRS}$ mice displayed numerous severe post-natal phenotypes. First, these knock-in mice were visibly smaller in size up to 7.5-months of age suggestive of a growth restriction phenotype (Figure 2A). *Srsf1*$^{NRS/NRS}$ mice were on average 30% lighter in weight than littermate controls (Student's t-test, $p<0.0001$). To investigate whether the growth restriction observed in *Srsf1*$^{NRS/NRS}$ mice arises during embryogenesis, E12.5 embryos and placentas were harvested from four *Srsf1*$^{+/NRS}$ intercross litters. *Srsf1*$^{NRS/NRS}$ embryos were grossly phenotypically normal at this stage of development (Figure 2B), with no difference in embryo or placenta weights compared to their *Srsf1*$^{+/+}$ (Figure 2C). These results indicate that the observed growth restriction does not arise from impaired embryogenesis or abnormal maternal nutrient transfer across the placenta, suggesting that postnatal growth is specifically affected in *Srsf1*$^{NRS/NRS}$ animals.

Srsf1$^{NRS/NRS}$ mice develop hydrocephalus

In addition to restricted growth, half of the *Srsf1*$^{NRS/NRS}$ animals developed clinically overt hydrocephalus by P14. In contrast, no cases of hydrocephalus were observed in either the *Srsf1*$^{+/+}$ or *Srsf1*$^{NRS/+}$ littermates (Figure 3A). Hydrocephalus is caused by the accumulation of cerebrospinal fluid (CSF) resulting in dilatation of brain ventricles and increased pressure on the surrounding brain tissue, which can lead to cranial doming during the perinatal period

((McAllister, 2012)(Figure 3A, upper panel). As in humans, hydrocephalus can result in progressive brain enlargement, neurological dysfunction, seizures and death.

Indeed, when we analyzed brain histology from both affected and unaffected mice, we observed clear evidence of subclinical hydrocephalus, as shown by dilatation of lateral and third ventricles, in *Srsf1*$^{NRS/NRS}$ mice that did not present external symptoms (Figure 3B, bottom-right panel). In some samples from visibly affected mutant mice, the accumulation of CSF resulted in compression and loss of brain tissue resulting from severe expansion of ventricular space (Figure 3B, top-right panel). In conclusion, our data indicates that *Srsf1*$^{NRS/NRS}$ mice develop hydrocephalus with variable severity that does not appear to be sex-linked (Table S1).

The SRSF1-NRS protein does not affect mRNA splicing or global mRNA export

SRSF1 is essential for cellular and organism viability, which has been attributed to its splicing role in the nucleus (Lin et al., 2005; Xu et al., 2005). The viability of *Srsf1*$^{NRS/NRS}$ knock-in mice, strongly suggests that SRSF1-mediated splicing was not grossly affected in the homozygous animals. In addition, previous work using an exogenous SRSF1-NRS protein revealed that the nuclear splicing role of SRSF1 was essential and could be decoupled from its ability to shuttle (Lin et al 2005). In order to confirm global RNA splicing was unaffected in primary cells expressing exclusively endogenous SRSF1-NRS, we performed deep RNA-sequencing analysis on mouse embryonic fibroblasts (MEF) lines derived from *Srsf1*$^{NRS/NRS}$, *Srsf1*$^{NRS/+}$ and *Srsf1*$^{+/+}$ littermates (Figure S3A, Table S2). Splicing changes were analyzed using SUPPA2, a tool which displays differential splicing between conditions as changes in proportion spliced-in (ΔPSI) (Trincado et al., 2018). As such, SUPPA2 is advantageous as it permits analysis of multiple samples and accounts for biological variability between samples. This was important as our biological replicates were isolated from different embryos with the same genotype, that will have a certain degree of intrinsic heterogeneity. Pairwise comparisons of *Srsf1*$^{+/+}$,

Srsf1$^{NRS/+}$ and *Srsf1*$^{NRS/NRS}$ MEFs demonstrated that there were no gross splicing changes induced by the presence of the NRS insertion (Figure S3A). Out of 65318 transcripts analyzed, we observed only 26 changes in splicing considering ΔPSI =>0.2 (p<=0.01), which is comparable to the number of changes between *Srsf1*$^{NRS/+}$ and *Srsf1*$^{+/+}$ MEFs. Considering that *Srsf1*$^{NRS/+}$ mice do not have a quantifiable phenotype, the changes we observe likely represent stochastic changes in alternative splicing that could be explained by environmental or sampling factors.

Shuttling SR proteins, including SRSF1, have been proposed to function in nuclear mRNA export, through interactions with the export factor TAP/NXF1 (Hargous et al., 2006; Huang and Steitz, 2001; Huang et al., 2003). We performed high-throughput RNA sequencing analysis on cytoplasmic fractions from MEFs derived from *Srsf1*$^{+/+}$ or *Srsf1*$^{NRS/NRS}$ animals or NSCs differentiated *in vitro* from ESCs derived from *Srsf1*$^{+/+}$ or *Srsf1*$^{NRS/NRS}$ animals (Figure S3B, Table S3). We found that the abundance of 121 and 57 mRNAs was decreased in the cytoplasm of *Srsf1*$^{NRS/NRS}$ MEFs and NSCs, respectively. In previous work, 225 transcripts were identified as the direct export targets of SRSF1 in P19 cells (Müller-McNicoll et al., 2016), however we found no overlap between their targets and mRNAs that change in this study. Similarly, cell fractionation followed by RT-qPCR of selected mRNAs in *Srsf1*$^{+/+}$ or *Srsf1*$^{NRS/NRS}$ cultures, revealed that the NRS insertion affected cytoplasmic levels of very few export candidates tested (Figure S3C). Taken together, our data shows that a nuclear restricted SRSF1 does not compromise pre-mRNA splicing and is associated with relatively few changes in mRNA export.

Shuttling SRSF1 is required for mRNA translation of a subset of transcripts

To determine whether the presence of a nuclear-retained SRSF1 protein affects mRNA translation *in vivo*, we performed polysomal shift analyses in different cell lines derived from

Srsf1$^{+/+}$ and *Srsf1*$^{NRS/NRS}$ animals. We selected ESCs as a pluripotent cell type, NSCs to explore changes upon differentiation into cellular types relevant to the observed phenotypes of *Srsf1*$^{NRS/NRS}$ animals, and MEFs as a primary cell type. Cytoplasmic RNA was harvested from three biological replicates and RNA-seq and polysomal profiling was carried out to measure the transcriptome and translatome, respectively (Figure 4A and Table S4). We confirmed the expression of the pluripotency gene *Oct4* (*Pou5f1*) in ESCs, whereas the co-expression of the neural stem cell markers *Nestin* (*Nes*) and *Sox2* in NSCs, indicated that the neural lineage has been successfully induced. Finally, *Thy1* was chosen as a fibroblast marker for MEF cultures (Table S3). Cytoplasmic extracts were fractionated across 10-45% sucrose gradients and RNA isolated from subpolysomal and heavy polysomal fractions, followed by high throughput sequencing, as previously described (Maslon et al., 2014). To accurately identify those mRNAs whose translation is responsive to the presence of cytoplasmic SRSF1 and remain associated with ribosomes during the fractionation procedure, we calculated polysome indices (PI) for each expressed gene, normalized to transcripts per million (TPM) and the polysome shift ratio (PSR) (PSR = log2(PI_SRSF1-NRS/PI_SRSF1)) between *Srsf1*$^{+/+}$ and *Srsf1*$^{NRS/NRS}$ cultures (see Methods). We used these values to determine transcripts that were significantly depleted ($p<0.05$) from polysomes in *Srsf1*$^{NRS/NRS}$ cells, as translation of such transcripts is likely to be directly compromised by the lack of shuttling SRSF1. This analysis revealed substantial changes in the association of mRNAs with polysomes in *Srsf1*$^{NRS/NRS}$ NSCs and MEFs, with a much lower proportion of changes in ESCs (Figure 4B). This analysis revealed a substantial loss in the number of mRNAs associated with polysomes in *Srsf1*$^{NRS/NRS}$ NSCs and MEFs, with a much lower proportion of changes in ESCs (Figure 4B). We found that 13 genes (total of 88) in ESCs, 1077 genes (total of 1258) in NSCs and 464 genes (total of 733) in MEFs were under-represented in the polysomal fractions of *Srsf1*$^{NRS/NRS}$ samples, strongly suggesting that SRSF1 is directly involved in their translation. When we compared translational changes considering

only genes commonly expressed in all three cell types (9073 in total), we observed that this had marginally affected the number of genes being affected in all three cell types (Figure S4). Therefore, the observed translational changes are not restricted to lineage specific transcripts but instead seem to correlate with ongoing differentiation programs or metabolic demands of each cell type. Overall, these results suggest that differentiating cells like NSCs and to a lesser extent MEFs, require SRSF1 for the translation of a subset of mRNAs. Interestingly, these SRSF1-dependent translational functions are dispensable in pluripotent cells like ESCs.

To confirm that the observed changes are indeed translational and not simply due to gene expression changes, we compared differences in alternative splicing and cytoplasmic RNA expression levels with the observed translational changes. Specifically, we compared genes with significantly different PSR between *Srsf1*$^{+/+}$ and *Srsf1*$^{NRS/NRS}$ cultures to their respective total mRNA and mRNA isoforms levels from RNA-seq data. Changes in polysome profiling and RNA levels did not correlate in either MEFs or NSCs (Figure S5A). This indicates that translational changes are a direct response to the loss of SRSF1 in cytoplasm rather than a consequence of altered transcription or mRNA export. Moreover, only a small fraction of differentially expressed splicing isoforms in the cytoplasm (Figure S5B) were found to differentially translated (Figure S5C). Overall, these findings show that the absence of SRSF1 from the cytoplasm has a major impact on translation and that these changes are dependent on the cell-type even though they primarily affect non-cell-type specific RNAs.

SRSF1 is required for the translation of cilia-related mRNA transcripts

Next, we performed gene ontology (GO) analysis to determine whether any functional gene category was differentially translated in SRSF1-NRS expressing cells (Figure 4C). We considered only transcripts with a change in PSR of >15%. From this analysis, we identified genes associated with spindle category as translationally downregulated in *Srsf1*$^{NRS/NRS}$ NSCs,

which agrees with our previous findings in SRSF1-overexpressing 293T cells (Maslon et al., 2014) and with the reduced body size of *Srsf1*$^{NRS/NRS}$ animals. Interestingly, the functional category related to motile cilium was also enriched among genes depleted from polysomal fractions of *Srsf1*$^{NRS/NRS}$ NSCs (Figure 4C). This is consistent with the hydrocephalus trait observed in *Srsf1*$^{NRS/NRS}$ animals, since this is caused by the abnormal accumulation of CSF in brain ventricles and is commonly found in animal models with dysfunctional motile cilia (Lee, 2013). Multiciliated ependymal cells line the ventricular walls of the brain and their concerted beating is required for cerebrospinal fluid (CSF) flow (reviewed in (Fliegauf et al., 2007)). Indeed, NSCs which can spontaneously differentiate in culture to multiciliated ependymal cells (Zvonic et al., 2007), express a number of mRNAs encoding motile cilia specific proteins and these were downregulated in *Srsf1*$^{NRS/NRS}$ NSCs polysome fractions (Figure 4D). We observed that dynein axonemal assembly factors *Dnaaf1/Lrrc50* and *Dnaaf3*, which are required for the functional assembly of axonemal dynein motors, as well as motor subunits themselves including those of both inner dynein arms (*i.e.* axonemal dynein heavy chain 7 (*Dnah7a*)) and outer dynein arms (*i.e.* dynein axonemal intermediate chain 2 (*Dnai2*)) were under-represented in the heavy polysome fractions of *Srsf1*$^{NRS/NRS}$ cultures. Together, these proteins form the functional macromolecular motors that drive ciliary movement, many of which are found mutated in patients with congenital dysfunction of motile cilia, termed primary ciliary dyskinesia (PCD) (Loges et al., 2008, 2009; Mitchison et al., 2012; Zhang et al., 2002). Importantly, the abundance of these mRNAs was not altered in the cytoplasm of *Srsf1*$^{NRS/NRS}$ cultures (Table S2), which was further confirmed by direct RT-PCR for *Dnaaf1* and *Dnaaf3* (Figure S3C). Altogether, this strongly suggests that SRSF1 participates in the translation of components of the motile cilia and could therefore directly underlie the phenotypes observed in *Srsf1*$^{NRS/NRS}$ pups. For these reasons we next focused on a detailed characterization of phenotypes associated with cilia motility in *Srsf1*$^{NRS/NRS}$ animals.

$Srsf1^{NRS/NRS}$ animals have compromised cilia motility

Congenital hydrocephalus is a relatively common anomaly of the central nervous system (CNS) (Dewan et al., 2019). Hydrocephalus can arise from obstruction of the aqueducts, by alterations in CSF production and/or absorption as well as by impaired flow of CSF (Ibañez-Tallon et al., 2004). Circulation of CSF within the CNS is dependent on ependymal cell cilia beating, particularly in rodents. To characterize the underlying cause of hydrocephalus in $Srsf1^{NRS/NRS}$ animals, we analyzed histological sections of postnatal animals and saw no malformation of aqueducts connecting the ventricles (Figure 5A). As both cilia from ependymal cells as well as cilia from choroid plexus are thought to contribute to cilia-related hydrocephalus in mice (Banizs et al., 2005; Ibañez-Tallon et al., 2004), $Srsf1^{NRS/+}$ animals were crossed onto a cilia cell cycle biosensor *ARL13B-Fucci2A* transgenic mice (Ford et al., 2018). Here, ubiquitous expression of the ciliary reporter ARL13B-Cerulean allows for live imaging of all ciliary types. Ependymal cilia of the lateral ventricles (Figure 5B) and the choroid plexus (Figure S6A) were directly examined upon dissection. Importantly, the motile cilia of $Srsf1^{NRS/NRS}$ animals formed regularly spaced bundles both in ependymal cells and choroid plexus, similar to those observed in controls. However, inspection of comparable regions of the lateral ventricles indicate that ciliary bundles of a young $Srsf1^{NRS/NRS}$ animal beat slower (Movie 1 and Figure 5C) and with different wave forms, compared to its control littermate (Figure 5D). The coordination between ciliary bundles of ependymal cells is important for CSF flow (Ibañez-Tallon et al., 2004; Takagishi et al., 2017), therefore the lower beat frequency and interspersed movement is likely to contribute to the hydrocephalus phenotype of $Srsf1^{NRS/NRS}$ animals.

Hydrocephalus and growth reduction are suggestive of PCD, this rare genetically heterogenous disorder caused by abnormal ciliary motility (Omran et al., 2008) is accompanied by male infertility due to abnormal sperm motility. In agreement, $Srsf1^{NRS/NRS}$ males presented smaller testes often with abnormal sperm morphology (Figure 5E) and mostly immotile

spermatozoa (Figure 5F). Phenotypic traits of *Srsf1*$^{NRS/NRS}$ animals are shared among mouse models for PCD, suggesting that defects in translation observed in *Srsf1*$^{NRS/NRS}$ mutants (Figure 4D) result in impaired function.

In order to pinpoint when defects in motile cilia function arise, we used proteomics, live cell imaging and transmission electron microscopy of mouse tracheal epithelial cultures (mTECs) derived from sets of *Srsf1*$^{NRS/NRS}$ and *Srsf1*$^{+/+}$ littermates. These synchronized primary cultures allow the stepwise study of the *de novo* production of multiciliated cells by exposure to air liquid interphase (ALI) and growth factors (Vladar and Brody, 2013). From progenitors bearing a single non-motile primary cilia to fully differentiated epithelial cells bearing hundreds of motile cilia, these cultures faithfully replicate airway developmental programs (Jain et al., 2010) during the course of a few weeks (Figure 6A and Methods section). These cultures allow us to observe unique features of motile ciliogenesis including the number of cilia formed by centriole amplification as well as changes in cilia content illustrated by movement parameters (Oltean et al., 2018). Motile cilia move randomly from the onset after the rapid burst of cytoplasmic synthesis, assembly and transport of motile specific components into apically docked cilia primordia, but their waveform changes as cilia matures and movement between ciliary bundles becomes coordinated propelling mucus across the surface of these multiciliated epithelia (Supplemental Figure 7A and Movie 2). The complexity and gradual waveform changes depend on multiple components not limited to ciliary motors, inner and outer dynein arms (IDA, ODA) that power ciliary beating, but also include structural support of motile axonemes (Tektins and Nexin-Dynein Regulatory complexes (N-DRC)) (Figure 6B), mutations in which are associated with PCD in patients (Loges et al., 2009; Mitchison et al., 2012; Wirschell et al., 2013) or animal models (Tanaka et al., 2004).

To investigate changes in protein levels during differentiation, we first performed unsupervised analyses of total proteomes from day 4 post-airlift (ALI4) to day 18 (ALI18) using

the subset of proteins, which have been annotated with the GO term cilia. We found some cilia candidates that were concurrently and significantly upregulated at later stages of differentiation in *Srsf1*$^{+/+}$ controls that failed to be induced in a coordinated manner in *Srsf1*$^{NRS/NRS}$ cultures (Figure 6C). Overall, the majority of changes between *Srsf1*$^{NRS/NRS}$ and *Srsf1*$^{+/+}$ proteomes involved downregulation of proteins with GO terms related to assembly of motile cilia (Supplemental Figure S7B and S7C). Interestingly, the affected proteins include dynein motor assembly factors (DNAAFs) and axonemal dynein motors (DNAHs), which were also seen under-represented in heavy polysome fractions of NSCs (Figure 4D), as well as Tektins and N-DRC components required for normal axoneme assembly and proper motility of mature ciliary bundles (Supplemental Figure S7D).

High-speed video microscopy and immunofluorescence of mTEC cultures during differentiation indicate that although the production of multiciliated cells is not affected (Figure S7E), a significant proportion of cilia remain immotile in *Srsf1*$^{NRS/NRS}$ inserts well until ALI13 (Figure 6D). Moreover, at these later stages, motile ciliary bundles still present altered beat patterns in relation to the control cultures, as illustrated by kymographs and ciliary beat frequencies (Figure 6E, 6F and Supplemental Figure S7F). Ultrastructural defects of cilia axonemes were observed in *Srsf1*$^{NRS/NRS}$ cells, including lack of central pair (1/81), three central microtubules (10/81) or single outer microtubules (2/81) compared to control *Srsf1*$^{+/+}$ cultures (1 single outer microtubule out of n= 94) (Figure 5G; X^2 of all microtubule defects < 0.001). These structural defects may be an underestimate, as not all axoneme abnormalities can be resolved by TEM, but those observed are consistent with the abnormal levels of motile cilia components found in *Srsf1*$^{NRS/NRS}$ proteomes.

In summary, we show that the *Srsf1*$^{NRS/NRS}$ mouse model mimics gross and cellular phenotypes attributable to defects in cilia motility, such as those observed in PCD patients. These phenotypic changes are consistent with the underlying alterations in translational status

of ciliary mRNA as well as altered proteomes and axonemal ultrastructure in *Srsf1*$^{NRS/NRS}$ animals. Taken together, we conclude that SRSF1 participates in the translational regulation of motile cilia components.

DISCUSSION

Shuttling SR proteins, including SRSF1, act to co-ordinate nuclear and cytoplasmic steps of gene expression (Änkö, 2014; Botti et al., 2017; Michlewski et al., 2008; Müller-McNicoll et al., 2016). Indeed, SRSF1 promotes translation of mRNAs encoding RNA processing factors and cell-cycle and centrosome-associated proteins in an mTOR-dependent manner (Fu et al., 2013; Maslon et al., 2014; Michlewski et al., 2008). However, despite increasing evidence for post-splicing activities of shuttling SR proteins, their physiological relevance has remained enigmatic. Here, we set out to comprehensively investigate the *in vivo* roles and requirement for cytoplasmic SRSF1. We created a mouse model in which SRSF1 is retained in the nucleus, by targeting a nuclear retention signal (NRS) to SRSF1 resulting in a fusion protein (SRSF1-NRS). In our model, abrogation of cytoplasmic SRSF1 function resulted in several deleterious phenotypes without affecting the nuclear roles of SRSF1.

Multiple postnatal phenotypic changes are observed in mice lacking cytoplasmic SRSF1

Srsf1$^{NRS/NRS}$ mice developed hydrocephalus with variable severity and were smaller than littermate counterparts. Homozygous males also had an increased proportion of immotile sperm, whilst those remaining, exhibit abnormal motility. Moreover, primary cells from both *Srsf1*$^{NRS/NRS}$ airways or brain ventricles displayed reduced cilia beat frequency and disturbed waveforms. These traits are characteristic of PCD, a genetically heterogenous disease of motile cilia (Lobo et al., 2015). Cilia are small microtubule-based projections found on the surface of most mammalian cells types. Defects in cilia function or structure result in a growing spectrum

of diverse human diseases known as the ciliopathies (Reiter and Leroux, 2017). Whilst we observed no gross phenotypes associated with defects in primary (immotile) cilia in *Srsf1*$^{NRS/NRS}$ animals, specific defects in the populations of motile cilia on cells lining brain ventricles, respiratory and reproductive tracts, as well as the sperm flagella, were observed. These motile cilia are essential to providing mechanical force to drive movement of fluids across a surface or a cell through fluid. The constellation of phenotypes, abnormal ciliary ultrastructure, altered proteomes and disrupted motility provide strong evidence that cytoplasmic functions for SRSF1 are essential *in vivo* during motile cilia differentiation.

Lack of cytoplasmic SRSF1 represses cilia-related mRNA transcripts

Independent experimental settings provide evidence that abrogation of the cytoplasmic function of SRSF1 led to a decreased polysomal association of a subset of mRNAs, yet its impact on alternative splicing (nuclear function of SRSF1) or on the abundance of target mRNAs in the cytoplasm (mRNA export) is minimal. This strongly suggests that mRNA translation is specifically debilitated when SRSF1 is absent from the cytoplasm. We found that the lack of cytoplasmic SRSF1 had little effect on translation in ESCs, but it affected translation of over one thousand genes in NSCs. These results are consistent with findings that human ESCs maintain low overall levels of translation, with a global increase in high polysomes upon differentiation towards neural lineages (Blair et al., 2017) and thus suggest that SRSF1 participates in developmental programs that rely heavily on translational control.

To further investigate the effects of depletion of cytoplasmic SRSF1 on the proteome, we used tracheal cultures as a model for the stepwise differentiation of motile ciliogenesis that could contribute to the phenotypes observed in *Srsf1*$^{NRS/NRS}$ animals. Given the link to SRSF1 dependent translation and mitotic functions at centrosomes in dividing cells (Maslon et al., 2014), it was possible that differentiation of multiciliated cells is impacted given the hundreds

of centrioles destined to become the basal bodies of motile cilia need to be generated within a single postmitotic cell (Meunier and Azimzadeh, 2016). In particular, depletion of mitotic oscillator component CDK1, previously shown to be a direct target of SRSF1 translation (Maslon et al., 2014), hinders differentiation of multiciliated ependymal cells at the stage of massive centriole production (Al Jord et al., 2017). However, in the absence of cytoplasmic SRSF1, differentiation appeared to occur on time and give rise to appropriately long multiciliated bundles (Figure S7E and S7F). However, cilia motility was specifically compromised, and protein levels of motile ciliary components were significantly reduced (Figure 6D). Furthermore, motility of the sperm flagella is also affected in *Srsf1*$^{NRS/NRS}$ animals (Figure 5F).

During multiciliogenesis, cells transition from bearing a single primary cilium to hundreds of motile cilia requiring *de novo* synthesis of millions of motor subunits and motile ciliary components in the correct stoichiometry within a short developmental window couple to ciliary elongation. Although a well-defined transcriptional code for induction of cilia motility exists, these transcriptional regulators of multiciliogenesis affect hundreds of motile ciliary genes (Lewis and Stracker, 2020) and lead to a drastic decrease in the production of ciliated bundles and cilia number per bundle (Gomperts et al., 2004). These traits were not observed in *Srsf1*$^{NRS/NRS}$ cultures. Recent evidence suggests the interesting possibility that spatially regulated translation may be occurring during motile ciliogenesis. During spermatogenesis, *Drosophila* mRNAs encoding motile ciliary proteins are stored in large cytoplasmic granules until their translation is required in the growing sperm axoneme, possibly regulating their translation (Fingerhut and Yamashita, 2020). In vertebrates, there is evidence of phase-separated cytoplasmic foci termed dynein axonemal particles (DynAPs) that contain assembly factors, chaperones and axonemal dynein proteins, that may provide a favorable environment for their orderly assembly and final transport onto cilia (Huizar et al., 2018). It remains to be

seen whether this is also the case for DynAPs, but as with most other phase-separated condensates, RNA is key to regulate the formation, size and composition of these phase transitions (Langdon et al., 2018; Maharana et al., 2018). It is possible that SRSF1 could contribute to localized mRNA delivery and/or translation at these cytoplasmic foci. It could promote the formation of mRNPs that confine such regulated transcripts until a timely co-translational assembly of these large protein complexes is required during motile ciliogenesis.

How and why is SRSF1 recruited to provide such a specific translation is currently not understood. An intriguing possibility is that SRSF1 is able to respond to metabolic demands of the cell needing to reshape its proteome during differentiation. We propose that SRSF1 is required for translation of mRNAs that are important for the execution of cilia motility programs, providing an extra regulatory level that will ensure responsive and scaleable translation at the peak demand of assembly of the complex motile cilia machinery.

In summary, we have developed the first mouse model that allowed us to assess the *in vivo* relevance of SRSF1 nucleo-cytoplasmic shuttling. We conclude that the presence of the splicing factor SRSF1 in the cytoplasm is essential for proper postnatal development, and this is mostly due to the effect of SRSF1 in mRNA translation, which critically affects target mRNAs involved in motile cilia biogenesis and function.

ACKNOWLEDGEMENTS

We thank Andrew Wood (MRC HGU) for discussion on CRISPR/Cas strategies, Lisa McKie for Histology work, the MRC Advanced Imaging Resource for expert advice and Jimi Wills for mass spectrometry sample preparation and analysis. Mass spectrometry was supported by the Wellcome Trust (Multiuser Equipment 208402/Z/17/Z). D.W. was supported by the Deutsche Forschungsgemeinschaft under Germany's Excellence Strategy – EXC2151 – 390873048 and J.N.H. by a PhD fellowship from the Boehringer Ingelheim Fonds. This work was supported by Core funding to the MRC Human Genetics Unit from the Medical Research Council (I.A, P.M., J.F.C). P.M was supported by an ERC Consolidator Grant 866355.

AUTHOR CONTRIBUTIONS

F.H., M.M.M, I.R.A. and J.F.C. conceived, designed, and interpreted the experiments. F.H., M.M.M. and P.L.Y. performed most of the experiments and data analysis. S.A. and N.B. provided all the bioinformatics analysis and statistical analysis. P.L.Y. and P.M. analyzed all the cilia phenotypes and contributed to discussion and interpretation of the results. J.N.H. and D.W. provided image analysis. A.vK. carried out mass spectrometry data and bioinformatic analysis. Edinburgh University Bioresearch & Veterinary Services performed CRISPR injections and mouse work. The manuscript was co-written by all authors.

DECLARATION OF INTERESTS

The authors have declared that no competing interests.

Figure 1

A)

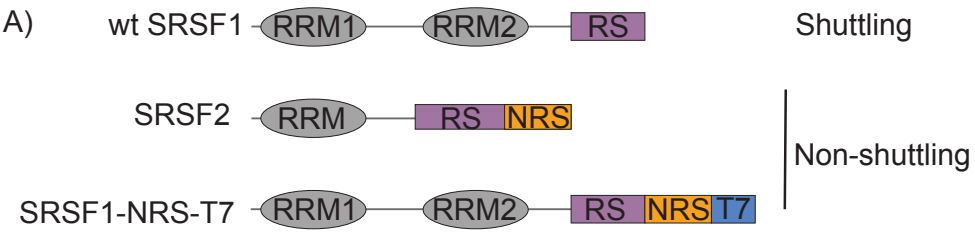

B)

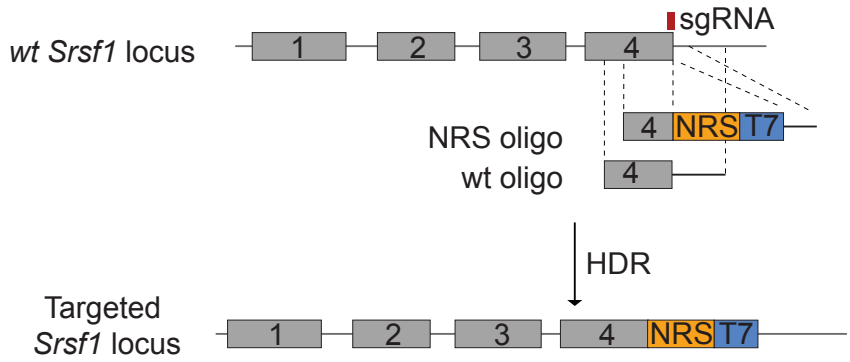

C)

Genotype	Observed	Expected
Srsf1 $^{+/+}$	17	17.25
Srsf1 $^{NRS/+}$	38	34.5
Srsf1 $^{NRS/NRS}$	14	17.25
Total	69	69
p-value	0.62	-

D)

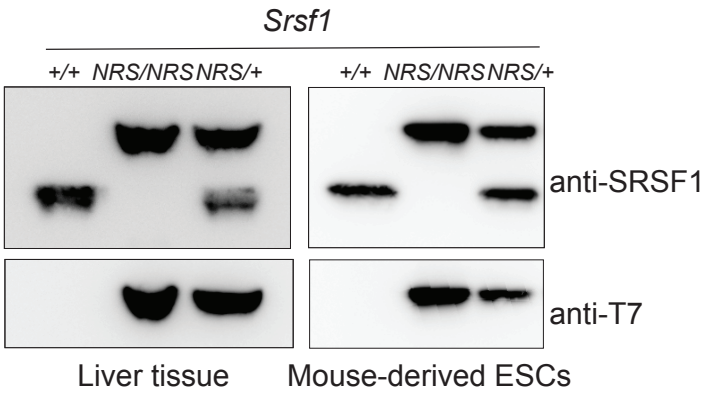

Figure 1. Generation of a nuclear restrained SRSF1 (*Srsf1*$^{NRS/NRS}$) knock-in mouse model

(A) Domain structure and nucleo-cytoplasmic shuttling ability of wild-type (WT) SRSF1 and SRSF2 proteins, and the artificial fusion protein SRSF1-NRS, used in this study.

(B) Schematic representation of the *Srsf1* locus and the CRISPR/Cas9 strategy used to introduce an NRS-T7 sequence at its C-terminus. The nucleotide sequence of the introduced NRS is identical to that present in the endogenous mouse *Srsf2* gene (Cazalla et al., 2002). Genotyping results are shown in Figure S1.

(C) *Srsf1*$^{NRS/NRS}$ homozygous knock-in mice can complete embryogenesis and are viable postnatally. The number of pups obtained from *Srsf1*$^{+/NRS}$ intercrosses with indicated genotypes at postnatal day 14 are indicated. The expected Mendelian numbers and χ^2-test P value (P=0.62, n=69) are also shown.

(D) Expression of the SRSF1-NRS protein from mouse liver tissue of three targeted mice (P14) (left panel) and in three ES cell lines derived from *Srsf1*$^{NRS/NRS}$ mice (right panel). In both panels, SRSF1 and T7 antibodies were used for Western blot analysis to detect the knock-in protein.

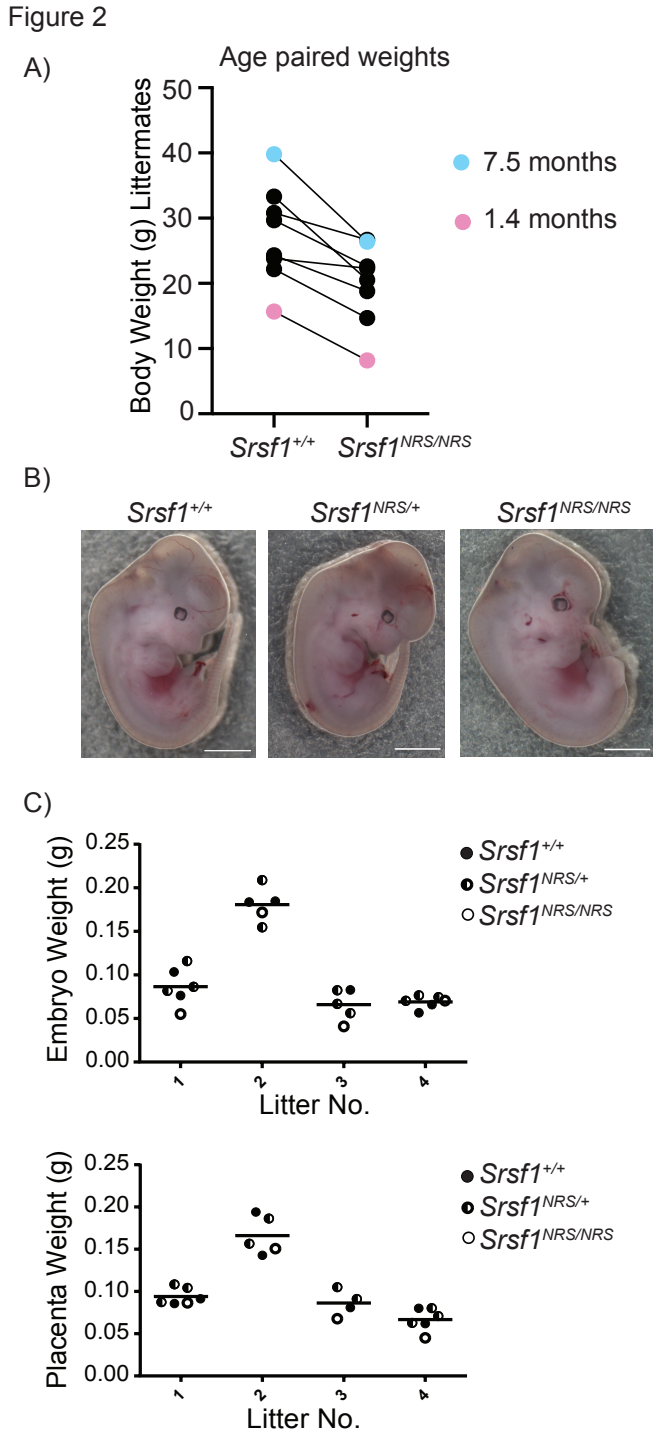

Figure 2. Homozygosity for the *Srsf1*^{NRS} allele causes postnatal growth restriction

(A) Whole body weight of sex-matched littermate pairs indicated by connecting lines. Animals range from 1.4 (pink) to 7.5 months old (blue).

(B) *Srsf1*$^{NRS/NRS}$ knock-in embryos at E13.5 are grossly phenotypically normal. *Srsf1*$^{NRS/NRS}$ embryos were represented in these litters at the expected Mendelian ratio (7 *Srsf1*$^{+/+}$, 11 *Srsf1*$^{+/NRS}$, 4 *Srsf1*$^{NRS/NRS}$; χ^2 P value=0.66).

(C) Scatter plots showing the weight of whole embryos (top panel) and of placentas from four independent litters of E12.5 embryos (bottom panel).

Figure 3

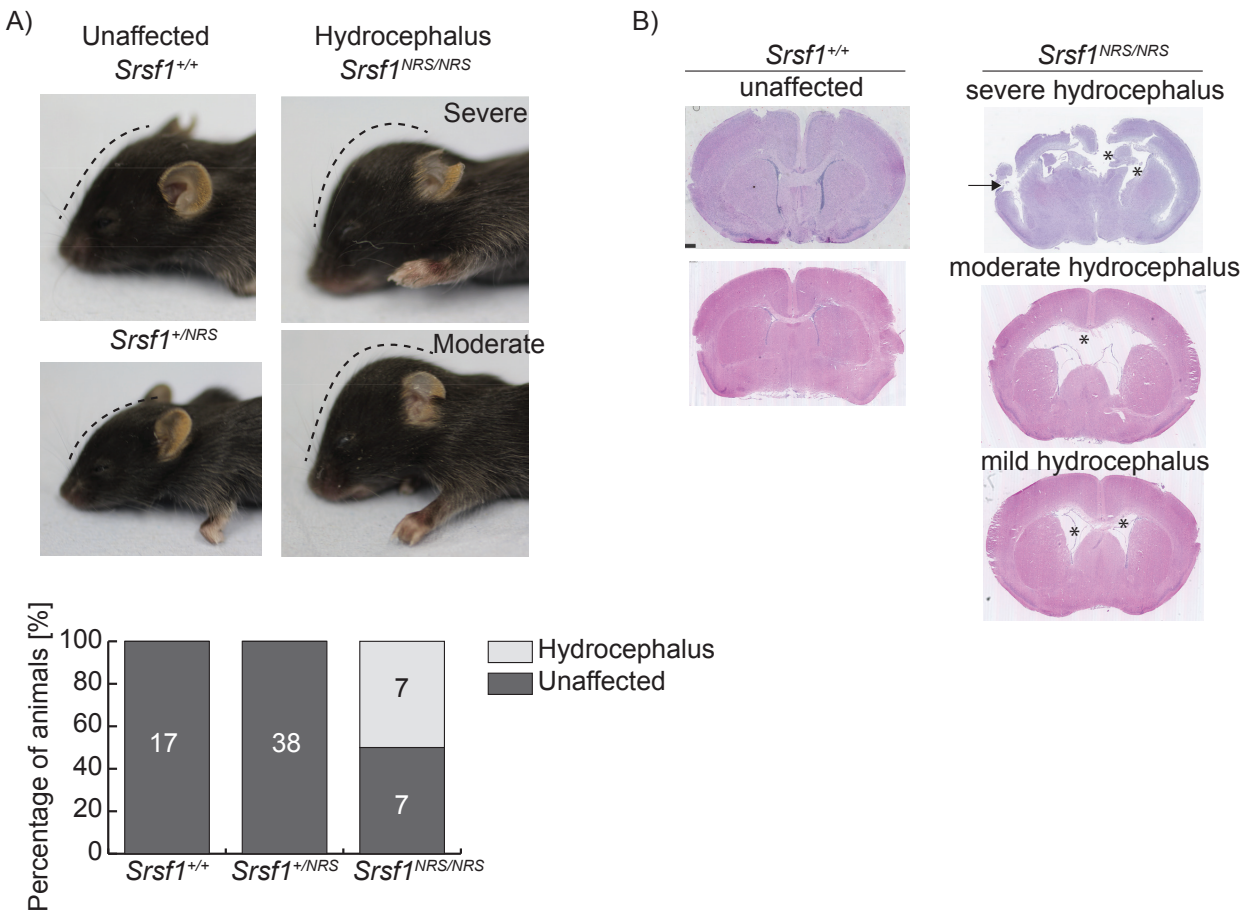

Figure 3. Homozygous *Srsf1*$^{NRS/NRS}$ mice develop hydrocephalus

(A) Homozygous *Srsf1*$^{NRS/NRS}$ mice show signs of developing hydrocephalus (the curvature of the skull is depicted by a dashed line). Half of the mice culled from the first two cohorts developed externally visible hydrocephalus of a varying severity by P14 (right panel), while hydrocephalus was not observed in *Srsf1*$^{+/+}$ or *Srsf1*$^{NRS/+}$ littermates (left panel). The barplot indicates the incidence of mice unaffected or with hydrocephalus (percentage and total number) in the 2 cohorts of mice used (p-value= 0.0013 and <0.0001, respectively; Fischer's exact test).

(B) Haemotoxylin and eosin (H&E) stained coronal brain sections taken from P14 mice to demonstrate the varying degrees of hydrocephalus in homozygous *Srsf1*^{NRS} knock-in mice. Note the expanded ventricles (*) and cortex deformation (arrows).

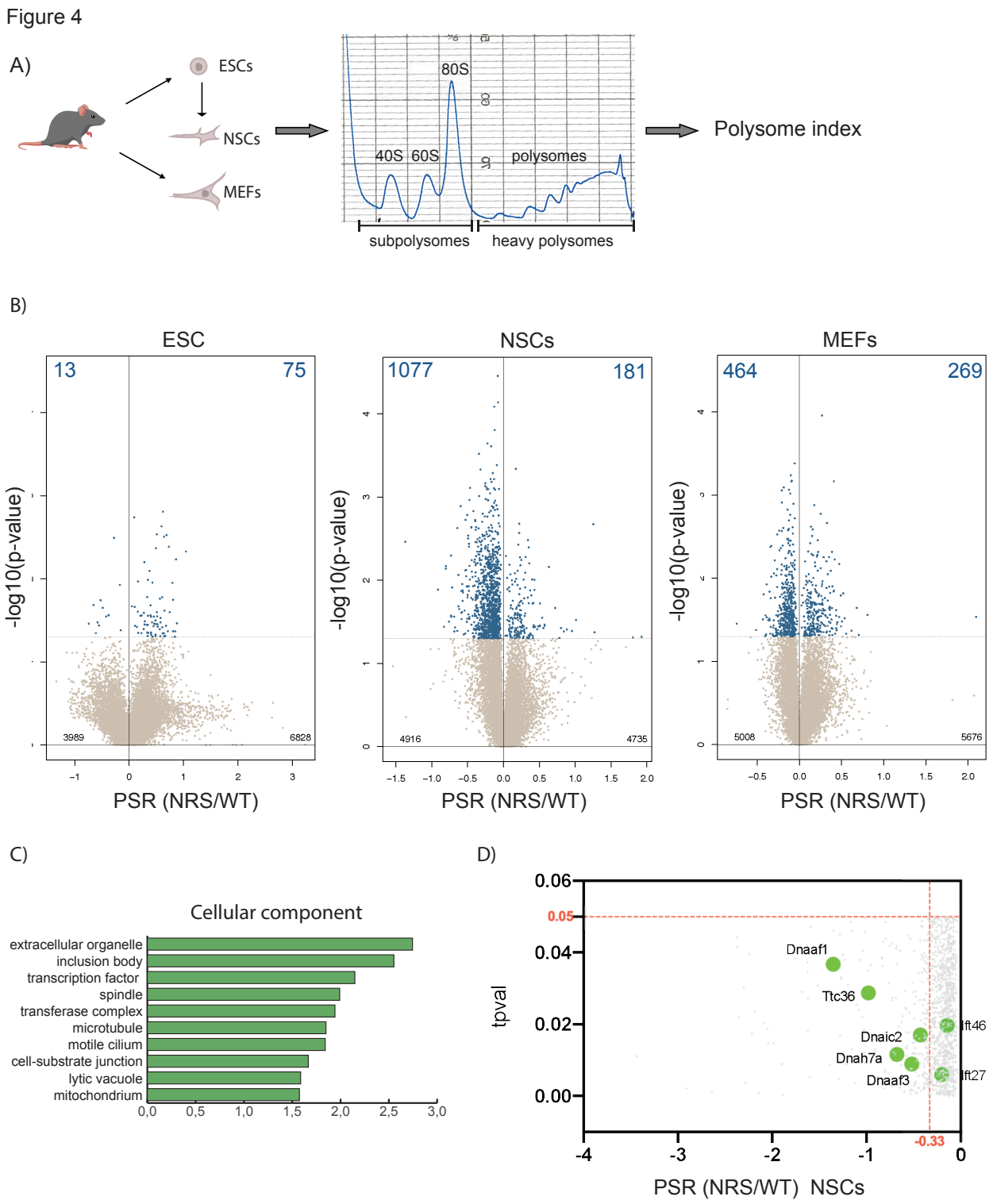

Figure 4. Lack of cytoplasmic SRSF1 results in gross changes in translation

(A) Schematic of the experimental approach used to identify translation profiles of wild-type SRSF1 or SRSF1-NRS-expressing ESCs, NSCs and MEF cells. A summary of a fractionation

profile is depicted. Absorbance at 254 nm was monitored. RNA isolated from the pooled subpolysomal and polysomal fractions was subjected to RNA sequencing.

(B) Scatter plots showing the distribution of genes expressed in all cell lines according to their polysome shift ratio (PSR). PSR is calculated as a ratio of polysome index in *Srsf1*$^{+/+}$ vs *Srsf1*$^{NRS/NRS}$ cells. Blue dots indicate significant changes. Number of significant changes is indicated in the top corners of each plot.

(C) GO term overrepresentation analysis identifies spindle and motile cilium as enriched cellular components category in the downregulated PSR gene list.

(D) Plot showing the distribution of genes expressed in NSCs with PSR<0. Selected cilial genes are highlighted.

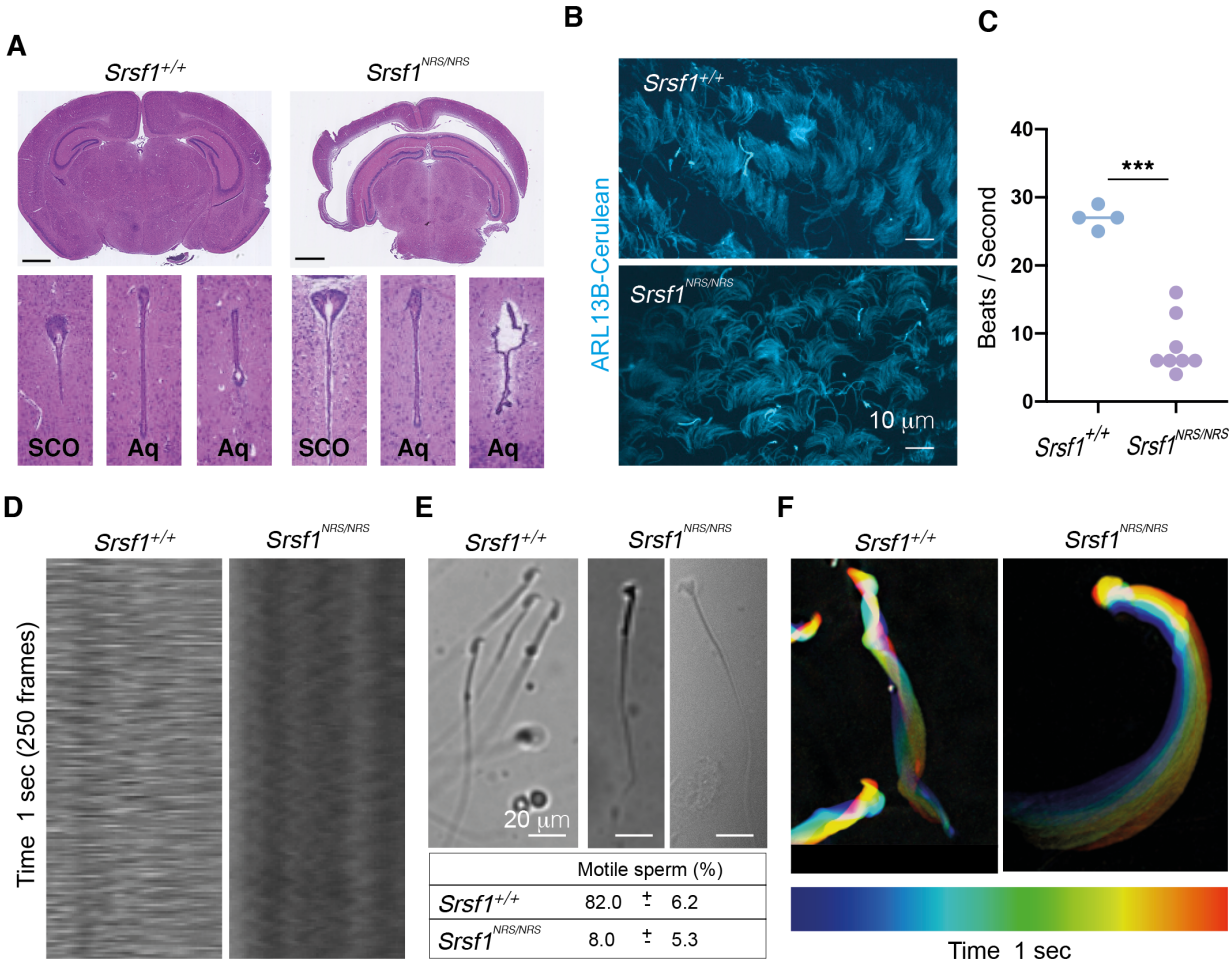

Figure 5. Phenotypes observed in ARL13B-Cerulean *Srsf1*$^{NRS/NRS}$ mice are consistent with defects in ciliary motility

(A) H&E staining of coronal sections of brains at subcommissural organ (SCO) and aqueducts (Aq) of 3rd and 4th ventricles show no obvert stenosis. Scale bar: 1 mm.

(B) Live images of ARL13B-Cerulean ependymal cells from the lateral ventricles showing comparable numbers of ciliary bundles between littermates although those of *Srsf1*$^{NRS/NRS}$ appear floppy.

(C) Frequency of ciliary beating from coronal sections along the lateral ventricles of P33 littermates.

(D) Kymographs of motile bundles illustrate differences in beating amplitude between littermates.

(E) Representative images illustrate abnormal head shape of spermatozoa observed in some *Srsf1*$^{NRS/NRS}$ littermates. Bottom panel shows percentage of motile sperm (N≥3 animals per genotype).

(F) Color coding illustrates that the complex rotational pattern of *Srsf1*$^{+/+}$ spermatozoa, required to propel the sperm forward, is absent in the few motile *Srsf1*$^{NRS/NRS}$ spermatozoa.

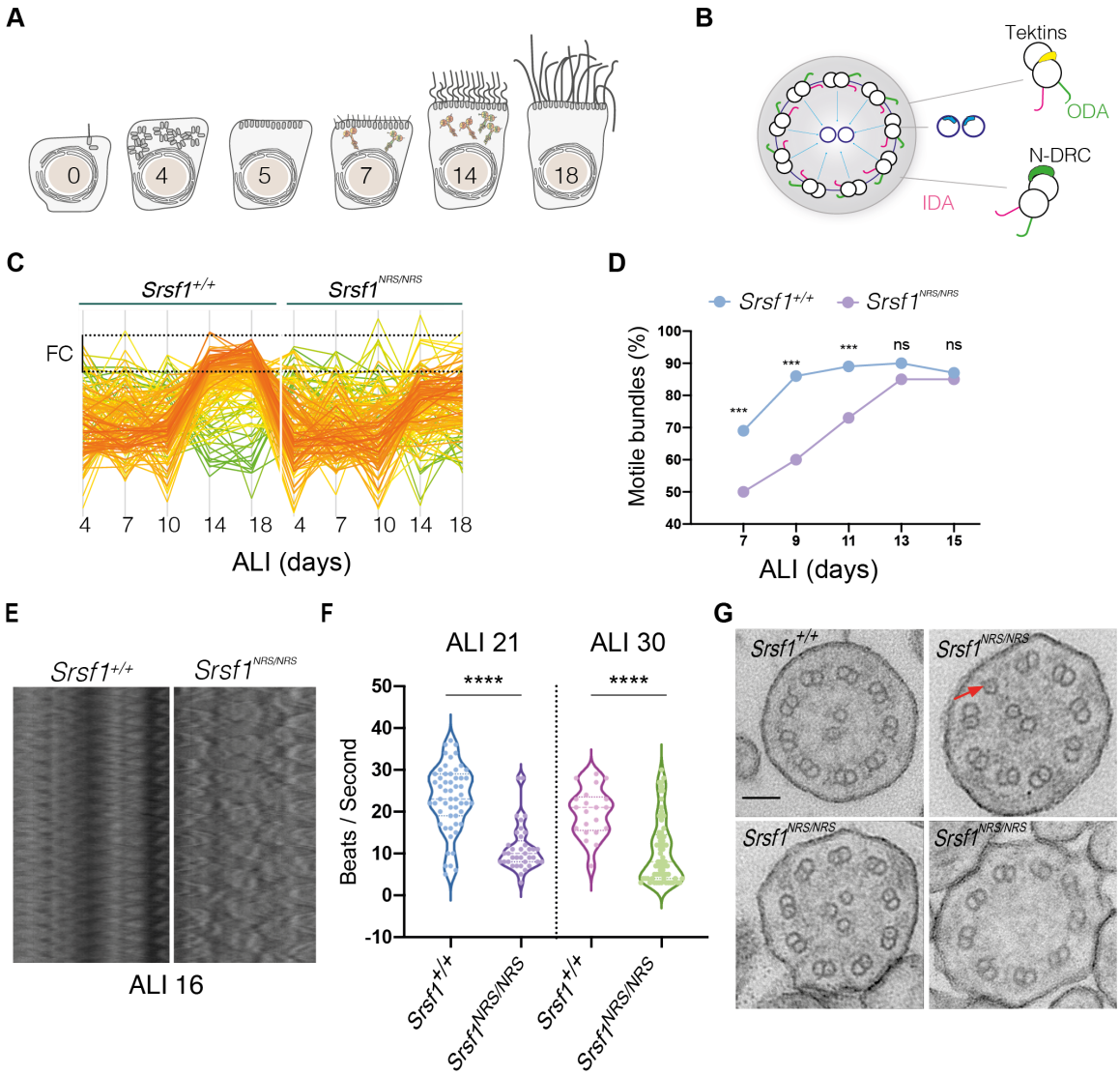

Figure 6. ARL13B-Cerulean *Srsf1*$^{NRS/NRS}$ mutants exhibit molecular and structural differences disrupting cilia motility

(A) Diagram depicts landmark events in the maturation of motile cilia in mTECs, upon culture as days post airlift (ALI). Stages depicted include centriole amplification and apical docking (ALI 4-6), synthesis and assembly of motile ciliary machinery concomitant with growth and ciliary elongation (ALI 7-14) continuous ciliary beat maturation (ALI 18).

(B) Diagram of motile specific components. N-DRC: nexin-dynein regulatory complexes, ODA: outer dynein arm IDA: inner dynein arm.

C) Z-normalized intensities of proteins containing "cilia" within their GO term aligned along tracheal stages (ALI4-18) and genotypes. Each line represents a single protein, where colour coding denotes those that match closely to the mean trajectory of the group (red) from those that deviate (green). This shows that *Srsf1*$^{+/+}$ induces the coordinated expression of multiple cilia-associated proteins during maturation with a greater amplitude that *Srsf1*$^{NRS/NRS.}$ Note the tighter distribution of trajectories, and greater fold change (FC) in *Srsf1*$^{+/+}$samples.

(D) Percentage of motile ciliary bundles during mTEC differentiation. N = 2 animals / genotype at ALI7 and ALI9; N=3 at all later stages. More than >100 ciliary bundles were scored at each time point. Asterisks represent p-value obtained from Chi square exact test at each stage.

(E) Representative kymographs of mTEC motile bundles illustrate differences in beating patterns at ALI16.

(F) Cilia beat frequency of a pair of animals/genotype during the indicated differentiation stages. Asterisks denote $p < 0.001$ determined by Mann Whitney tests as *Srsf1*$^{NRS/NRS}$ ciliary movement do not follow a normal distribution.

(G) Transmission electron microscopy of transverse sections of mTEC cilia showing (9+2) microtubules in *Srsf1*$^{+/+}$ or abnormal variations found in *Srsf1*$^{NRS/NRS}$. Red arrow illustrates microtubule singlet. Scale bar: 100 nm.

REFERENCES

Anczuków, O., Rosenberg, A.Z., Akerman, M., Das, S., Zhan, L., Karni, R., Muthuswamy, S.K., and Krainer, A.R. (2012). The splicing factor SRSF1 regulates apoptosis and proliferation to promote mammary epithelial cell transformation. Nat. Struct. Mol. Biol. *19*, 220–228.

Änkö, M.-L. (2014). Regulation of gene expression programmes by serine–arginine rich splicing factors. Semin. Cell Dev. Biol. *32*, 11–21.

Banizs, B., Pike, M.M., Millican, C.L., Ferguson, W.B., Komlosi, P., Sheetz, J., Bell, P.D., Schwiebert, E.M., and Yoder, B.K. (2005). Dysfunctional cilia lead to altered ependyma and choroid plexus function, and result in the formation of hydrocephalus. Development *132*, 5329–5339.

Baralle, F.E., and Giudice, J. (2017). Alternative splicing as a regulator of development and tissue identity. Nat. Rev. Mol. Cell Biol. *18*, 437–451.

Bedard, K.M., Daijogo, S., and Semler, B.L. (2007). A nucleo-cytoplasmic SR protein functions in viral IRES-mediated translation initiation. EMBO J. *26*, 459–467.

Blair, J.D., Hockemeyer, D., Doudna, J.A., Bateup, H.S., and Floor, S.N. (2017). Widespread Translational Remodeling during Human Neuronal Differentiation. Cell Rep. *21*, 2005–2016.

Botti, V., McNicoll, F.F., Steiner, M.C., Richter, F.M., Solovyeva, A., Wegener, M., Schwich, O.D., Poser, I., Zarnack, K., Wittig, I., et al. (2017). Cellular differentiation state modulates the mRNA export activity of SR proteins. J. Cell Biol. *216*, 1993–2009.

Busch, A., and Hertel, K.J. (2012). Evolution of SR protein and hnRNP splicing regulatory factors. Wiley Interdiscip. Rev. RNA *3*, 1–12.

Cáceres, J.F., Misteli, T., Screaton, G.R., Spector, D.L., and Krainer, A.R. (1997). Role of the modular domains of SR proteins in subnuclear localization and alternative splicing specificity. J. Cell Biol. *138*, 225–238.

Cáceres, J.F., Screaton, G.R., and Krainer, A.R. (1998). A specific subset of SR proteins shuttles continuously between the nucleus and the cytoplasm. Genes Dev. *12*, 55–66.

Cazalla, D., Zhu, J., Manche, L., Huber, E., Krainer, A.R., and Caceres, J.F. (2002). Nuclear Export and Retention Signals in the RS Domain of SR Proteins. Mol. Cell. Biol. *22*, 6871–6882.

Cléry, A., Sinha, R., Anczuków, O., Corrionero, A., Moursy, A., Daubner, G.M., Valcárcel, J., Krainer, A.R., and Allain, F.H.-T. (2013). Isolated pseudo-RNA-recognition motifs of SR proteins can regulate splicing using a noncanonical mode of RNA recognition. Proc. Natl. Acad. Sci. U. S. A. *110*, E2802-11.

Cong, L., Ran, F.A., Cox, D., Lin, S., Barretto, R., Habib, N., Hsu, P.D., Wu, X., Jiang, W., Marraffini, L.A., et al. (2013). Multiplex genome engineering using CRISPR/Cas systems. Science *339*, 819–823.

Cowper, A.E., Cáceres, J.F., Mayeda, A., and Screaton, G.R. (2001). Serine-arginine (SR) protein-like factors that antagonize authentic SR proteins and regulate alternative splicing. J. Biol. Chem. *276*, 48908–48914.

Crichton, J.H., Playfoot, C.J., MacLennan, M., Read, D., Cooke, H.J., and Adams, I.R. (2017). Tex19.1 promotes Spo11-dependent meiotic recombination in mouse spermatocytes. PLOS Genet. *13*, e1006904.

Czechanski, A., Byers, C., Greenstein, I., Schrode, N., Donahue, L.R., Hadjantonakis, A.K., and Reinholdt, L.G. (2014). Derivation and characterization of mouse embryonic stem cells from permissive and nonpermissive strains. Nat. Protoc. *9*, 559–574.

Dewan, M.C., Rattani, A., Mekary, R., Glancz, L.J., Yunusa, I., Baticulon, R.E., Fieggen, G., Wellons, J.C., Park, K.B., and Warf, B.C. (2019). Global hydrocephalus epidemiology and incidence: Systematic review and meta-analysis. J. Neurosurg. *130*, 1065–1079.

Dobin, A., Davis, C.A., Schlesinger, F., Drenkow, J., Zaleski, C., Jha, S., Batut, P., Chaisson, M., and Gingeras, T.R. (2013). STAR: Ultrafast universal RNA-seq aligner. Bioinformatics *29*, 15–21.

Fingerhut, J.M., and Yamashita, Y.M. (2020). mRNA localization mediates maturation of cytoplasmic cilia in Drosophila spermatogenesis. J. Cell Biol. *219*, e202003084.

Fliegauf, M., Benzing, T., and Omran, H. (2007). When cilia go bad: Cilia defects and ciliopathies. Nat. Rev. Mol. Cell Biol. *8*, 880–893.

Ford, M.J., Yeyati, P.L., Mali, G.R., Keighren, M.A., Waddell, S.H., Mjoseng, H.K., Douglas, A.T., Hall, E.A., Sakaue-Sawano, A., Miyawaki, A., et al. (2018). A Cell/Cilia Cycle Biosensor for Single-Cell Kinetics Reveals Persistence of Cilia after G1/S Transition Is a General Property in Cells and Mice. Dev. Cell *47*, 509-523.e5.

Fu, X.-D., and Ares, M. (2014). Context-dependent control of alternative splicing by RNA-binding proteins. Nat. Rev. Genet. *15*, 689–701.

Fu, Y., Huang, B., Shi, Z., Han, J., Wang, Y., Huangfu, J., and Wu, W. (2013). SRSF1 and SRSF9 RNA binding proteins promote Wnt signalling-mediated tumorigenesis by enhancing β-catenin biosynthesis. EMBO Mol. Med. *5*, 737–750.

Gomperts, B.N., Gong-Cooper, X., and Hackett, B.P. (2004). Foxj1 regulates basal body anchoring to the cytoskeleton of ciliated pulmonary epithelial cells. J. Cell Sci. *117*, 1329–1337.

Gui, J.F., Lane, W.S., and Fu, X.D. (1994). A serine kinase regulates intracellular localization of splicing factors in the cell cycle. Nature *369*, 678–682.

Hanamura, A., Cáceres, J.F., Mayeda, A., Franza, B.R., and Krainer, A.R. (1998). Regulated tissue-specific expression of antagonistic pre-mRNA splicing factors. RNA *4*, 430–444.

Hansen, J., Rassmann, S., Jikeli, J., and Wachten, D. (2018). SpermQ–A Simple Analysis Software to Comprehensively Study Flagellar Beating and Sperm Steering. Cells *8*, 10.

Hargous, Y., Hautbergue, G.M., Tintaru, A.M., Skrisovska, L., Golovanov, A.P., Stevenin, J., Lian, L.-Y., Wilson, S.A., and Allain, F.H.-T. (2006). Molecular basis of RNA recognition and TAP binding by the SR proteins SRp20 and 9G8. EMBO J. *25*, 5126–5137.

Howard, J.M., and Sanford, J.R. (2015). The RNAissance family: SR proteins as multifaceted regulators of gene expression. Wiley Interdiscip. Rev. RNA *6*, 93–110.

Huang, Y., and Steitz, J.A. (2001). Splicing factors SRp20 and 9G8 promote the nucleocytoplasmic export of mRNA. Mol. Cell *7*, 899–905.

Huang, Y., and Steitz, J.A. (2005). SRprises along a messenger's journey. Mol. Cell *17*, 613–615.

Huang, Y., Gattoni, R., Stévenin, J., and Steitz, J.A. (2003). SR splicing factors serve as adapter proteins for TAP-dependent mRNA export. Mol. Cell *11*, 837–843.

Huizar, R.L., Lee, C., Boulgakov, A.A., Horani, A., Tu, F., Marcotte, E.M., Brody, S.L., and Wallingford, J.B. (2018). A liquid-like organelle at the root of motile ciliopathy. Elife *7*, e38497.

Ibañez-Tallon, I., Pagenstecher, A., Fliegauf, M., Olbrich, H., Kispert, A., Ketelsen, U.P., North, A., Heintz, N., and Omran, H. (2004). Dysfunction of axonemal dynein heavy chain Mdnah5 inhibits ependymanl flow and reveals a novel mechanism for hydrocephalus formation. Hum. Mol. Genet. *13*, 2133–2141.

Jain, R., Pan, J., Driscoll, J.A., Wisner, J.W., Huang, T., Gunsten, S.P., You, Y., and Brody, S.L. (2010). Temporal relationship between primary and motile ciliogenesis in airway epithelial cells. Am. J. Respir. Cell Mol. Biol. *43*, 731–739.

Al Jord, A., Shihavuddin, A., D'Aout, R.S., Faucourt, M., Genovesio, A., Karaiskou, A., Sobczak-Thépot, J., Spassky, N., and Meunier, A. (2017). Calibrated mitotic oscillator drives motile ciliogenesis. Science (80-.). *358*, 803–806.

Joyner, A.L. (2000). Gene targeting : a practical approach (Oxford University Press).

Karni, R., de Stanchina, E., Lowe, S.W., Sinha, R., Mu, D., and Krainer, A.R. (2007). The gene encoding the splicing factor SF2/ASF is a proto-oncogene. Nat. Struct. Mol. Biol. *14*, 185–193.

Kataoka, N., Bachorik, J.L., and Dreyfuss, G. (1999). Transportin-SR, a nuclear import receptor for SR proteins. J. Cell Biol. *145*, 1145–1152.

Katsuyama, T., Li, H., Comte, D., Tsokos, G.C., and Moulton, V.R. (2019). Splicing factor SRSF1 controls T cell hyperactivity and systemic autoimmunity. J. Clin. Invest. *129*, 5411–5423.

Lai, M.C., Lin, R.I., Huang, S.Y., Tsai, C.W., and Tarn, W.Y. (2000). A human importin-beta family protein, transportin-SR2, interacts with the phosphorylated RS domain of SR proteins. J. Biol. Chem. *275*, 7950–7957.

Langdon, E.M., Qiu, Y., Niaki, A.G., McLaughlin, G.A., Weidmann, C.A., Gerbich, T.M., Smith, J.A., Crutchley, J.M., Termini, C.M., Weeks, K.M., et al. (2018). mRNA structure determines specificity of a polyQ-driven phase separation. Science (80-.). *360*, 922–927.

Lee, L. (2013). Riding the wave of ependymal cilia: Genetic susceptibility to hydrocephalus in primary ciliary dyskinesia. J. Neurosci. Res. *91*, 1117–1132.

Lewis, M., and Stracker, T.H. (2020). Transcriptional regulation of multiciliated cell differentiation. Semin. Cell Dev. Biol. S1084-9521(19)30187-9.

Liao, Y., Wang, J., Jaehnig, E.J., Shi, Z., and Zhang, B. (2019). WebGestalt 2019: gene set analysis toolkit with revamped UIs and APIs. Nucleic Acids Res. *47*, W199–W205.

Lin, S., Xiao, R., Sun, P., Xu, X., and Fu, X.-D. (2005). Dephosphorylation-dependent sorting of SR splicing factors during mRNP maturation. Mol. Cell *20*, 413–425.

Lobo, J., Zariwala, M.A., and Noone, P.G. (2015). Primary ciliary dyskinesia. Semin. Respir. Crit. Care Med. *36*, 169–179.

Loges, N.T., Olbrich, H., Fenske, L., Mussaffi, H., Horvath, J., Fliegauf, M., Kuhl, H., Baktai, G., Peterffy, E., Chodhari, R., et al. (2008). DNAI2 Mutations Cause Primary Ciliary Dyskinesia with Defects in the Outer Dynein Arm. Am. J. Hum. Genet. *83*, 547–558.

Loges, N.T., Olbrich, H., Becker-Heck, A., Häffner, K., Heer, A., Reinhard, C., Schmidts, M., Kispert, A., Zariwala, M.A., Leigh, M.W., et al. (2009). Deletions and Point Mutations of LRRC50 Cause Primary Ciliary Dyskinesia Due to Dynein Arm Defects. Am. J. Hum. Genet. *85*, 883–889.

Long, J.C., and Caceres, J.F. (2009). The SR protein family of splicing factors: master regulators of gene expression. Biochem. J. *417*, 15–27.

Love, M.I., Huber, W., and Anders, S. (2014). Moderated estimation of fold change and dispersion for RNA-seq data with DESeq2. Genome Biol. *15*, 550.

Maharana, S., Wang, J., Papadopoulos, D.K., Richter, D., Pozniakovsky, A., Poser, I., Bickle, M., Rizk, S., Guillén-Boixet, J., Franzmann, T.M., et al. (2018). RNA buffers the phase separation behavior of prion-like RNA binding proteins. Science (80-.). *360*, 918–921.

Mahiet, C., and Swanson, C.M. (2016). Control of HIV-1 gene expression by SR proteins. Biochem. Soc. Trans. *44*, 1417–1425.

Maslon, M.M., Heras, S.R., Bellora, N., Eyras, E., and Cáceres, J.F. (2014). The translational landscape of the splicing factor SRSF1 and its role in mitosis. Elife *3*, e02028.

Maslon, M.M., Braunschweig, U., Aitken, S., Mann, A.R., Kilanowski, F., Hunter, C.J., Blencowe, B.J., Kornblihtt, A.R., Adams, I.R., and Cáceres, J.F. (2019). A slow transcription rate causes embryonic lethality and perturbs kinetic coupling of neuronal genes. EMBO J. *38*, e101244.

McAllister, J.P. (2012). Pathophysiology of congenital and neonatal hydrocephalus. Semin. Fetal Neonatal Med. *17*, 285–294.

Meunier, A., and Azimzadeh, J. (2016). Multiciliated cells in animals. Cold Spring Harb. Perspect. Biol. *8*, a028233.

Michlewski, G., Sanford, J.R., and Cáceres, J.F. (2008). The splicing factor SF2/ASF regulates translation initiation by enhancing phosphorylation of 4E-BP1. Mol. Cell *30*, 179–189.

Mitchison, H.M., Schmidts, M., Loges, N.T., Freshour, J., Dritsoula, A., Hirst, R.A., O'Callaghan, C., Blau, H., Al Dabbagh, M., Olbrich, H., et al. (2012). Mutations in axonemal dynein assembly factor DNAAF3 cause primary ciliary dyskinesia. Nat. Genet. *44*, 381–389.

Möröy, T., and Heyd, F. (2007). The impact of alternative splicing in vivo: Mouse models show the way. RNA *13*, 1155–1171.

Müller-McNicoll, M., Botti, V., de Jesus Domingues, A.M., Brandl, H., Schwich, O.D., Steiner, M.C., Curk, T., Poser, I., Zarnack, K., and Neugebauer, K.M. (2016). SR proteins are NXF1 adaptors that link alternative RNA processing to mRNA export. Genes Dev. *30*, 553–566.

Naftelberg, S., Schor, I.E., Ast, G., and Kornblihtt, A.R. (2015). Regulation of Alternative Splicing Through Coupling with Transcription and Chromatin Structure. Annu. Rev. Biochem. *84*, 165–198.

Ngo, J.C.K., Giang, K., Chakrabarti, S., Ma, C.-T., Huynh, N., Hagopian, J.C., Dorrestein, P.C., Fu, X.-D., Adams, J.A., and Ghosh, G. (2008). A sliding docking interaction is essential for sequential and processive phosphorylation of an SR protein by SRPK1. Mol. Cell *29*, 563–576.

Olstad, E.W., Ringers, C., Hansen, J.N., Wens, A., Brandt, C., Wachten, D., Yaksi, E., and Jurisch-Yaksi, N. (2019). Ciliary Beating Compartmentalizes Cerebrospinal Fluid Flow in the Brain and Regulates Ventricular Development. Curr. Biol. *29*, 229-241.e6.

Oltean, A., Schaffer, A.J., Bayly, P. V., and Brody, S.L. (2018). Quantifying ciliary dynamics during assembly reveals stepwise waveform maturation in airway cells. Am. J. Respir. Cell Mol. Biol. *59*, 511–522.

Omran, H., Kobayashi, D., Olbrich, H., Tsukahara, T., Loges, N.T., Hagiwara, H., Zhang, Q., Leblond, G., O'Toole, E., Hara, C., et al. (2008). Ktu/PF13 is required for cytoplasmic pre-assembly of axonemal dyneins. Nature *456*, 611–616.

Park, J.W., Tokheim, C., Shen, S., and Xing, Y. (2013). Identifying differential alternative splicing events from RNA sequencing data using RNASeq-MATS. Methods Mol. Biol. *1038*, 171–179.

Patro, R., Duggal, G., Love, M.I., Irizarry, R.A., and Kingsford, C. (2017). Salmon provides fast and bias-aware quantification of transcript expression. Nat. Methods *14*, 417–419.

Piñol-Roma, S., and Dreyfuss, G. (1992). Shuttling of pre-mRNA binding proteins between nucleus and cytoplasm. Nature *355*, 730–732.

Prasad, J., Colwill, K., Pawson, T., and Manley, J.L. (1999). The protein kinase Clk/Sty directly modulates SR protein activity: both hyper- and hypophosphorylation inhibit splicing. Mol. Cell. Biol. *19*, 6991–7000.

Reiter, J.F., and Leroux, M.R. (2017). Genes and molecular pathways underpinning ciliopathies. Nat. Rev. Mol. Cell Biol. *18*, 533–547.

Saldi, T., Cortazar, M.A., Sheridan, R.M., and Bentley, D.L. (2016). Coupling of RNA polymerase II transcription elongation with pre-mRNA splicing. J. Mol. Biol. *428*, 2623–2635.

Sanford, J.R., Gray, N.K., Beckmann, K., and Cáceres, J.F. (2004). A novel role for shuttling SR proteins in mRNA translation. Genes Dev. *18*, 755–768.

Sanford, J.R., Ellis, J.D., Cazalla, D., and Cáceres, J.F. (2005). Reversible phosphorylation differentially affects nuclear and cytoplasmic functions of splicing factor 2/alternative splicing factor. Proc. Natl. Acad. Sci. U. S. A. *102*, 15042–15047.

Sapra, A.K., Ankö, M.-L., Grishina, I., Lorenz, M., Pabis, M., Poser, I., Rollins, J., Weiland, E.-M., and Neugebauer, K.M. (2009). SR protein family members display diverse activities in the formation of nascent and mature mRNPs in vivo. Mol. Cell *34*, 179–190.

Schindelin, J., Arganda-Carreras, I., Frise, E., Kaynig, V., Longair, M., Pietzsch, T., Preibisch, S., Rueden, C., Saalfeld, S., Schmid, B., et al. (2012). Fiji: An open-source platform for biological-image analysis. Nat. Methods *9*, 676–682.

Sun, S., Zhang, Z., Sinha, R., Karni, R., and Krainer, A.R. (2010). SF2/ASF autoregulation involves multiple layers of post-transcriptional and translational control. Nat. Struct. Mol. Biol. *17*, 306–312.

Swartz, J.E., Bor, Y.-C., Misawa, Y., Rekosh, D., and Hammarskjold, M.-L. (2007). The shuttling SR protein 9G8 plays a role in translation of unspliced mRNA containing a constitutive transport element. J. Biol. Chem. *282*, 19844–19853.

Takagishi, M., Sawada, M., Ohata, S., Asai, N., Enomoto, A., Takahashi, K., Weng, L., Ushida, K., Ara, H., Matsui, S., et al. (2017). Daple Coordinates Planar Polarized Microtubule Dynamics in Ependymal Cells and Contributes to Hydrocephalus. Cell Rep. *20*, 960–972.

Tanaka, H., Iguchi, N., Toyama, Y., Kitamura, K., Takahashi, T., Kaseda, K., Maekawa, M., and Nishimune, Y. (2004). Mice Deficient in the Axonemal Protein Tektin-t Exhibit Male Infertility and Immotile-Cilium Syndrome Due to Impaired Inner Arm Dynein Function. Mol. Cell. Biol. *24*, 7958–7964.

Trincado, J.L., Entizne, J.C., Hysenaj, G., Singh, B., Skalic, M., Elliott, D.J., and Eyras, E. (2018). SUPPA2: fast, accurate, and uncertainty-aware differential splicing analysis across multiple conditions. Genome Biol. *19*, 40.

Twyffels, L., Gueydan, C., and Kruys, V. (2011). Shuttling SR proteins: more than splicing factors. FEBS J. *278*, 3246–3255.

Tyanova, S., Temu, T., Sinitcyn, P., Carlson, A., Hein, M.Y., Geiger, T., Mann, M., and Cox, J. (2016). The Perseus computational platform for comprehensive analysis of (prote)omics data. Nat. Methods *13*, 731–740.

Ule, J., and Blencowe, B.J. (2019). Alternative Splicing Regulatory Networks: Functions, Mechanisms, and Evolution. Mol. Cell *76*, 329–345.

Vladar, E.K., and Brody, S.L. (2013). Analysis of ciliogenesis in primary culture mouse tracheal epithelial cells. In Methods in Enzymology, (Academic Press Inc.), pp. 285–309.

Wang, J., Takagaki, Y., and Manley, J.L. (1996). Targeted disruption of an essential vertebrate gene: ASF/SF2 is required for cell viability. Genes Dev. *10*, 2588–2599.

Wegener, M., and Müller-McNicoll, M. (2019). View from an mRNP: The Roles of SR Proteins in Assembly, Maturation and Turnover. Adv. Exp. Med. Biol. *1203*, 83–112.

Wirschell, M., Olbrich, H., Werner, C., Tritschler, D., Bower, R., Sale, W.S., Loges, N.T., Pennekamp, P., Lindberg, S., Stenram, U., et al. (2013). The nexin-dynein regulatory complex subunit DRC1 is essential for motile cilia function in algae and humans. Nat. Genet. *45*, 262–268.

Xu, X., Yang, D., Ding, J.-H., Wang, W., Chu, P.-H., Dalton, N.D., Wang, H.-Y., Bermingham, J.R., Ye, Z., Liu, F., et al. (2005). ASF/SF2-regulated CaMKIIdelta alternative splicing temporally reprograms excitation-contraction coupling in cardiac muscle. Cell *120*, 59–72.

Zhang, Y.J., O'Neal, W.K., Randell, S.H., Blackburn, K., Moyer, M.B., Boucher, R.C., and Ostrowski, L.E. (2002). Identification of dynein heavy chain 7 as an inner arm component of human cilia that is synthesized but not assembled in a case of primary ciliary dyskinesia. J. Biol. Chem. *277*, 17906–17915.

Zhou, Z., and Fu, X.-D. (2013). Regulation of splicing by SR proteins and SR protein-specific kinases. Chromosoma *122*, 191–207.

Zhu, J., Mayeda, A., and Krainer, A.R. (2001). Exon identity established through differential antagonism between exonic splicing silencer-bound hnRNP A1 and enhancer-bound SR proteins. Mol. Cell *8*, 1351–1361.

Zvonic, S., Lefevre, M., Kilroy, G., Floyd, Z.E., DeLany, J.P., Kheterpal, I., Gravois, A., Dow, R., White, A., Wu, X., et al. (2007). Secretome of primary cultures of human adipose-derived stem cells: Modulation of serpins by adipogenesis. Mol. Cell. Proteomics *6*, 18–28.

KEY RESOURCES TABLE

REAGENT OR RESOURCE	SOURCE	IDENTIFIER
Antibodies		
SRSF1	Mouse monoclonal 96 (Hanamura *et al*. 1998)	n/a
T7	Novagen	69522
Chemicals, Recombinant Proteins		
Trizol	Life Technologies	15596026
Q5 High-Fidelity DNA polymerase	New England Biolabs	M0491
Cas9	TriLink BioTechnologies	L7606
Hoechst 34580	Sigma Aldrich	63493
Cycloheximide	Sigma Aldrich	C104450
PEG1500	Roche	10783641001
Cell culture reagents, cytokines		
Lipofectamine 3000	Thermo Fisher Scientific	L3000015
Recombinant Murine EGF	Peprotech	315-09
Recombinant Human FGF-basic	Peprotech	100-18B
MEM Non-essential amino acid	Gibco	11140050
Sodium pyruvate	Gibco	11360070
2-mercaptoethanol	Gibco	31350010
Accutase	Stemcell	
BSA (7.5% solution)	Thermo Scientific	15260037
Laminin	Sigma Aldrich	L2020
N-2 Supplement (100x)	Thermo Scientific	17502048
B-27 Supplement (50x)	Thermo Scientific	17504044
PD0325901	Stemcell Technologies	72182
CHIR99021	Miltenyi Biotec	130-103-926
Commercial Assays and Kits		
RNeasy kit	Qiagen	74106
Turbo DNase	Ambion	AM1907
SybrGreen RT-QPCR	Roche	04707516001
T7 Quick High Yield RNA Synthesis kit	NEB	E2050S
Experimental Models: **Cell lines/Strains**		
ESCs *Srsf1*$^{NRS/NRS}$	This paper	n/a
NSCs *Srsf1*$^{NRS/NRS}$	This paper	n/a
MEFs *Srsf1*$^{NRS/NRS}$	This paper	n/a
Srsf1$^{NRS/NRS}$	This paper	MGI: 6452080

Software and algorithms		
R (v3.5)	N/A	https://www.r-project.org/
STAR	(Dobin et al., 2013)	http://code.google.com/p/rna-star/.
Salmon	(Patro et al., 2017)	https://combine-lab.github.io/salmon/
SUPPA2	(Trincado et al., 2018)	https://github.com/comprna/SUPPA.
WebGestalt2019	(Liao et al., 2019)	http://www.webgestalt.org/
MATS	(Park et al., 2013)	http://rnaseq-mats.sourceforge.net/
DESeq2	(Love et al., 2014)	http://www.bioconductor.org/ packages/release/bioc/html/DESeq2.html
SpermQ	(Hansen et al., 2018)	https://github.com/hansenjn/SpermQ
FIJI	(Schindelin et al., 2012)	https://imagej.net/Fiji
MaxQuant 1.6	N/A	(https://www.maxquant.org/)
Perseus	(Tyanova et al., 2016)	https://maxquant.net/perseus/
GraphPad Prism 8	N/A	https://www.graphpad.com/
Deposited data		
Polysomal profiling RNA-seq data	This paper	http://181.89.68.25:8080/94d277f fb060705f65f4fb94a1fbcf98/
MEFs RNA-seq data	This paper	GSE157269
mTECs proteomics data	This paper	PXD019859, username: reviewer79803@ebi.ac.uk password: 4HAr4wOY.

LEAD CONTACT AND MATERIALS AVAILABILITY

Further information and requests for resources and reagents should be directed to and will be fulfilled by the Lead Contact, Javier F. Caceres (Javier.Caceres@igmm.ed.ac.uk)

Materials and Methods

Animal experiments

We followed international, national and institutional guidelines for the care and use of animals. Animal experiments were carried out under UK Home Office Project Licenses PPL 60/4424, PB0DC8431 and P18921CDE in facilities at the University of Edinburgh (PEL 60/2605) and were approved by the University of Edinburgh animal welfare and ethical review body.

CRISPR/Cas9 Gene Editing in Mouse Zygotes

The CRISPR target sequence (20-nucleotide sequence followed by a protospacer adjacent motif (PAM) of 'NGG') were selected using the prediction software (http://www.broadinstitute.org/rnai/public/analysis-tools/sgrna-design). Single gRNAs targeting exon 4 of *Srsf1* (Srsf1-205, ENSMUST00000139129.8) were annealed and cloned into the PX458 plasmid (Cong et al., 2013). The guide region was then amplified by PCR and paired guide RNAs synthesised by in vitro transcription (T7 Quick High Yield RNA Synthesis kit, NEB). Single stranded DNA oligonucleotides (WT oligo: "CGTAGCAGAAGCAACAGCAGGAGTCGCAGTTACTCCCCAAGGAGAAGCAGAGG ATCACCACGCTATTCTCCCCGTCATAGCAGATCTCGCTCTCGTACATAAGATGATT GATGACACTTTTTGTAGAACCCATGTTGTATACAGTTTTCCTTTACTCAGTACAAT CTTTTCATTTTTTTAATTCAAGCTGTTTTGTTCAG", NRS oligo: "AAGCAGAGGATCACCACGCTATTCTCCCCGTCATAGCAGATCTCGCTCTCGTACA GGATCCCCTCCGCCCGTGTCGAAGCGAGAGTCCAAGTCTAGGTCGCGGTCCAAGA GCCCACCCAAGTCTCCAGAAGAAGAGGGAGCAGTTTCTTCCATGGCATCGATGAC AGGTGGCCAACAGATGGGTTAAGATGATTGGTGACACTTTTTGTAGAACCCATGT TGTATACAGTTTTCCTTTACTC" and T7 oligo:

"TTACTCCCCAAGGAGAAGCAGAGGATCACCACGCTATTCTCCCCGTCATAGCAG ATCTCGCTCTCGTACAGGAT**CCCCCGGCGCCGGCG**CCATGGCATCG ATGACAGGTGGCCAACAGATGGGTTAAGATGATTGGTGACACTTTTTGTA GAACCCATGTTGTATACAGTTTTCCTTTACTCAGTACAATCTTTTCA") were synthesized by IDT. The sequence encoding a small peptide linker (P-G-A-G-A), inserted between the NRS and the T7 peptide, is highlighted in bold. Gene editing was performed by microinjection of RNA encoding the wild-type Cas9 nuclease (50 ng/µl, TriLink BioTechnologies), 25 ng/µl single guide RNA (sgRNA) targeting exon 4 of *Srsf1*, and 150 ng/µl of both NRS-T7 and WT single-stranded DNA oligonucleotides of a similar length containing 50-100 nucleotides of homology flanking both sides of the sgRNA as repair templates into (C57BL/6 x CBA) F2 zygotes (Crichton et al., 2017). The injected zygotes were cultured overnight in KSOM for subsequent transfer to the oviduct of pseudopregnant recipient females (Joyner, 2000). From microinjection CRISPR targeting, 57 pups were born, and genomic DNA from ear-clip tissue was subject to PCR screening and subsequent sequence verification of successful mutagenesis events by Sanger sequencing (Figure S1). Two heterozygous founder mice were each backcrossed for one generation to C57BL/6 wild type mice to allow unwanted allelic variants to segregate. Of the resulting 32 pups, 10 animals, were confirmed by sequencing to be heterozygous for the correct SRSF1-NRS allele (Figure S1B, Allele Accession ID: MGI:6452080) and subsequently intercrossed. The phenotypes reported in Figs. 1-3 were present in *Srsf1*$^{NRS/NRS}$ animals derived from both independent founder mice, confirming their association with homozygosity for *SRSF1*^{NRS} rather than an off-target or spontaneous mutation. Genotyping was performed by PCR using the following forward and reverse primers:

TTGATGGGCCCAGAAGTCC and ATAGGGCCCTCTAGACAATTTCATCTGTGACAATAGC, respectively.

$Srsf1^{NRS}$; ARL13B-Cerulean biosensor mice

The ubiquitously expressing ARL13B-Cerulean biosensor was established by crossing our tricistronic reporter line *R26Arl13b-Fucci2aR*$^{Tg/+}$ to CAG-Cre$^{+/TG}$ driver (Ford et al., 2018) and maintained on a mixed background as a homozygous stock facilitating rapid derivation of compound mutant animals. *Srsf1*$^{NRS/+}$ and *ARL13B-Fucci2A*$^{Tg/Tg}$ animals were crossed accordingly to obtain the *Srsf1*$^{NRS/NRS}$ mutants used to visualize ependymal and choroid plexus cilia and kept in that genetic background for subsequent ciliary studies. In this background *Srsf1*$^{NRS/NRS}$ mutants were born at the frequencies of 32 *Srsf1*$^{+/+}$, 75 *Srsf1*$^{+/NRS}$, 27 *Srsf1*$^{NRS/NRS}$. The genotyping of the compound animals was done by TransNetyx.

Cell cultures

ESCs were grown on gelatin-coated plates in 2i media (1:1 Neurobasal and DMEM/F12, supplemented with 0.5X N2, 0.5x B27, 0.05% BSA, 1M PD0325901, 3M CHIR99021, 2mM L-glutamine, 0.15mM monothioglycerol, 100U/ml LIF). NSCs were grown on laminin-coated plates in DMEM/F12 medium supplemented with 2mM L-glutamine, 0.5x N2, B27, glucose, BSA, HEPES and 10ng/ml of both mouse EGF and human FGF-2. MEFs were cultured in Dulbecco's Modified Eagle's Medium (DMEM) supplemented with 10% fetal bovine serum (FBS).

Derivation and maintenance of ESCs

Embryonic stem cells were established from *Srsf1*$^{NRS/+}$ x *Srsf1*$^{NRS/+}$ crosses, following an adapted version of the protocol by (Czechanski et al., 2014). E3.5 blastocysts were isolated and

plated in 4-well plates pre-seeded with Mitomycin-C-treated MEFs. All derivation and downstream propagation of established lines was carried out in 2i media. After the first 48 h during which the blastocysts were undisturbed, media was changed every other day. Outgrowths were isolated after approximately one week and transferred to a fresh feeder-coated plate. Successfully derived cells were slowly weaned from feeders by continual passaging before genotyping to avoid contamination of genomic DNA.

Neuroectodermal specification

ESCs were cultured under feeder-free conditions in 2i medium. One day prior to induction of differentiation cells were seeded at high density in 2i medium. The following day, cells were detached using Accutase, resuspended in N2B27 media (1:1 Neurobasal and DMEM/F12, supplemented with 0.5X N2, 0.5x B27, 0.1 mM 2-mercaptoethanol, 0.2 mM L-glutamine), counted and plated at approximately 10,000 cells per cm^2 onto either 15 cm plates or 6 well plates that have been coated with a 0.1% gelatin solution. Culture medium was changed every second day.

Deriving NS cells

For derivation of neural stem cells at day 7 of differentiation, cultures were detached using Accutase, 2-3 x 10^6 cells were re-plated into an uncoated T75 flask in NS expansion media, comprising DMEM/F12 medium supplemented with 2mM L-glutamine, 0.5x N2, B27, glucose, BSA, HEPES and 10ng/ml of both mouse EGF (Peprotech) and human FGF-2 (Peprotech). Within 2-3 days, thousands of cell aggregates formed in suspension culture and were harvested by centrifugation at 700 rpm for 1 min. They were then re-plated onto a laminin coated T75 flask. After few days, cell aggregates attached to the flask and outgrew with NS cell.

Heterokaryon assay

This was performed as previously described (Cazalla et al., 2002; Piñol-Roma and Dreyfuss, 1992), with minor modifications. Donor mouse NSCs were seeded on laminin-coated cover slips, followed by co-incubation with an excess of HeLa cells (recipient) for 3 h in the presence of 50 µg/ml cycloheximide, to prevent further protein synthesis in the heterokaryons. The concentration of cycloheximide was then increased to 100 µg/ml, and the cells were incubated for an additional 30 min prior to fusion. Cells were fused with PEG1500 in the presence of 100 µg/ml cycloheximide and the heterokaryons were further incubated for 3 h in media containing 100 µg/ml. Cells were then fixed and stained with a T7 antibody, and DNA was stained with Hoechst 33258 to distinguish between mouse and human nuclei.

Mouse tracheal epithelial cultures

These were established as described previously (Vladar and Brody, 2013). *Srsf1*$^{+/+}$ and *Srsf1*$^{NRS/NRS}$ animals were always sacrificed as pairs. Tracheas were dissected and dissociated individually. More than 5 pairs of animals were used to establish tracheal cultures used along this study. Cells were expanded into monolayers of progenitor cells in T25 flasks until confluency and dissociated as described to be seeded onto 6-9 transwells of 6.5 mm each depending on cell density. Under these conditions, our cultures have roughly no ciliary bundles until day 4 and visibly motile cilia until day 7, reaching mature coordinated beating between adjacent bundles by 25-30 days post- airlifting. Membranes of transwells were released from inserts and inverted onto a glass bottom plate for imaging after which cells were harvested for proteomics, immunofluorescence or electron microscopy.

RNA isolation and RT-qPCR

RNA was isolated using TRIzol or RNAeasy following the manufacturer's protocol. RNA was then treated with Dnase (Ambion) and transcribed to cDNA using First-Strand Synthesis System from Roche. This was followed by SybrGreen detection system (Lightcycler 2x SybrGreen Mix, Roche).

Cell fractionation and sucrose gradient centrifugation

ESCs, MEFs, or NSCs were treated with 50 µg/ml cycloheximide for 30 min. Cells were subsequently washed twice in ice-cold PBS containing cycloheximide. Cytoplasmic extracts were prepared as previously described (Sanford et al., 2004). Sucrose gradients (10-45%) containing 20mM Tris, pH 7.5, 5mM $MgCl_2$, 100mM KCl were made using the BioComp gradient master. Extracts were loaded onto the gradient and centrifuged for 2.5 h at 41,000 rpm in Sorvall centrifuge with SW41Ti rotor. Following centrifugation, gradients were fractionated using a BioComp gradient station model 153 (BioComp Instruments, Inc. New Brunswick, Canada) measuring cytosolic RNA at 254 nm. Fractions eight to eleven (polysomal fractions) and one to seven (subpolysomal fraction) were pooled and diluted sucrose concentration adjusted to 20%. The RNA extraction was performed as described above.

RNA-Seq analysis

RNA-sequencing was carried out on RNA extracted from *Srsf1*$^{+/+}$, *Srsf1*$^{NRS/+}$ or *Srsf1*$^{NRS/NRS}$ MEFs. RNA was purified using RNeasy kit from three independent experiments. RNA-seq libraries were generated from Poly(A)$^{+}$ mRNA using TrueSeq protocol and sequenced using the Illumina Hi-Seq 4000 machine (WTCRF Edinburgh) to generate 75 bases, paired-end reads. Reads were mapped to the mouse (mm10) genome. Paired reads were pseudoaligned to the GRCm38 (mm10) Ensembl 87 transcriptome using salmon (Patro et al., 2017). Splicing

changes were inferred from transcript TPMs using SUPPA2 (Trincado et al., 2018) from gene definitions in the Ensembl 87. SUPPA2 infers splicing changes (dPSI) from changes in transcript models across the two conditions being compared. These results were filtered on mean transcript expression (TPM>0.5).

Polysomal shift analysis

Experiments were performed in three biological replicates. Monosomal, polysomal and cytoplasmic reads were mapped to the mouse genome sequence (mm10) by STAR software (Dobin et al., 2013) (v2.0.7f) with –outFilterScoreMinOverLread 0.3 –outFilterMatchNminOverLread 0.3settings and Ensembl release M21 transcript annotation. Polysomal Indexes (PIs) were calculated for each condition for the set of protein coding genes based on a procedure previously described (Maslon et al., 2014). The transcript abundance metric, RPKM, was replaced by transcripts per million reads (TPMs) as such normalization allows comparison between samples without biases. The PIs and associated polysomal shift ratios (PSRs) were calculated for each sample by pooling reads from replicates. The statistical significance of PSRs were assessed by Student's t-Test on the variability of PIs of individual replicates. Alternative splicing events were retrieved using rMATS (v3.2.5) (Park et al., 2013). The results were filtered by a minimum coverage of 10 reads per junction and replicate, dPSI>0.2 and FDR<0.05. Differential expression analysis was performed with DEseq2 (v1.26.0) (Love et al., 2014) and results were filtered by FDR<0.05.

Gene Ontology analysis

GO term enrichment analysis was performed using WebGestalt2019 (Liao et al., 2019). Genes downregulated at least 0.85-fold (PSR<=-0.23) or upregulated at least 1.15-fold were used as an input. The following parameters were used for the enrichment analysis: minimum number

of IDs in the category: 5 and maximum number of IDs in the category: 300

Protein extraction, antibodies and Western Blotting

Cell pellets were lysed in 50 mM Tris pH8.0, 150 mM NaCl, 1 % NP-40 buffer containing protease inhibitors. Protein samples either from ESCs or liver extracts were separated by SDS-PAGE and electroblotted onto nitrocellulose membranes (Whatman) using iblot System for 6 min (Invitrogen). Non-specific binding sites were blocked by incubation of the membrane with 5 % nonfat milk in PBS containing 0.1% Tween 20 (PBST). Proteins were detected using the following primary antibodies diluted in blocking solution: mouse monoclonal anti-SRSF1 (clone 96; 1:1000 (Hanamura et al., 1998)), mouse monoclonal anti-tubulin (Sigma (T8328)) and mouse monoclonal anti-T7 (Novagen, 1:10,000. Following washing in PBST, blots were incubated with the appropriate secondary antibodies conjugated to horse-radish peroxidase (Pierce) and detected with Super Signal West Pico detection reagent (Pierce).

Proteomics

Each transwell (1 experimental replicate) of mTECs cultures were lysed in 350 µl of PBS, 2% SDS and antiproteolytic cocktail, kept at -80°C until all time points were harvested to be run simultaneously. Total proteomes were derived from two animals/genotype with 3 experimental replicate per time point (Day 4 to 10, animal pair 1; day 14 to 18 animal pair two). Cell lysates were digested using sequential digestion of LysC (Wako) and trypsin (Pierce) using the FASP protocol (https://pubmed.ncbi.nlm.nih.gov/25063446/). Samples were acidified to 1% TFA final volume and clarified by spinning on a benchtop centrifuge (15k g, 5 min). Sample clean-up to remove salts was performed using C18 stage-tips [PMID: 12585499]. Samples were eluted in 25 µl of 80% Acetonitrile containing 0.1% TFA and dried using a SpeedVac system at 30°C and resuspended in 0.1% (v/v) TFA such that each sample contained 0.2 µg/ml. All

samples were run on an Orbitrap FusionTM Lumos mass spectrometer coupled to an Ultimate 3000, RSL-Nano uHPLC (both Thermo Fisher). 5 ul of the samples were injected onto an Aurora column (25 cm, 75um ID Ionoptiks, Australia) and heated to 50C. Peptides were separated by a 150 min gradient from 5-40% Acetonitrile in 0.5% Acetic acid. Data were acquired as data-dependent acquisition with the following settings: MS resolution 240k, cycle time 1 s, MS/MS HCD ion-trap rapid acquisition, injection time 28ms. The data were analyzed using the MaxQuant 1.6 software suite (https://www.maxquant.org/) by searching against the murine Uniprot database with the standard settings enabling LFQ determination and matching. The data were further analyzed using the Perseus software suite. LFQ values were normalized, 0-values were imputed using a normal distribution using the standard settings. To generate expression profiles of cilium-related proteins, gene ontology annotations were added and all entries containing "cilia" were retained. Expression profiles were normalized (using Z-score) and expression profiles were plotted.

Histology

Whole brains from P14 mice were embedded in paraffin wax and 5μM sections cut using a microtome before oven drying overnight at 60°C. Sections were dewaxed in xylene and rehydrated in decreasing concentrations of ethanol with a final rinse in running water. Sections were stained in haematoxylin for 4 min, rinsed in water then placed in 1% HCl in 70% EtOH for 5 sec before rinsing again in water and treating with Lithium carbonate solution for 5 sec. Tissue sections were rinsed well in running water for 5 min and stained in Eosin for 2 min before rinsing in water and washing three times in 100% EtOH for 1 min each. Sections were cleared in fresh xylene 3 times for 5 min and mounted using DPX mounting media.

Live cell Imaging

Brains were dissected under dissection microscope in the presence of high glucose DMEM supplemented with 10% FCS to preserve cell viability. Fluorescence live imaging of ependymal and choroid plexus tissue was performed on a Nikon A1R confocal microscope with relevant laser lines and band filters for ARL13B-Cerulean (Ford et al., 2018). Data was acquired using either a 40x Plan Fluar 0.75 DIC N2 or 60x Plan Apochromat VC 1.2 WI DIC N2 lens through Andor software with spinning disk in 25 μm pinhole mode on the high sensitivity iXon888 EMCCD camera. Data was visualized using IMARIS 8.4 (Bitplane). Brightfield imaging with high speed camera was acquired using NIS Elements Software (Nikon Instruments Europe, Netherlands) with a region of interest of 520 x 520 in 11-bit mode 1 frame, to acquire 250 frames/second. In all cases, tissues were immersed in imaging media (high glucose DMEM and 10% FCS) and imaged at room temperature within 2 h post-mortem.

Cilia motility analysis

For the assessment of motility, movies of ciliary bundles were imaged randomly as they appeared on the field of view. Motile vs immotile bundles during mTEC maturation were scored by direct visual inspection of these movies. The number of all counts for each category at each time point were used to calculate the significance of the different proportions between *Srsf1*$^{NRS/NRS}$ and *Srsf1*$^{+/+}$ cultures by Fisher Exact test. Other parameters of cilia motility were analyzed in FIJI as indicated in each panel by slowing down animation to manually count beats/sec of distinct ciliary bundles or automatically by the custom-written ImageJ plugin "Cilility_JNH" (available upon request). The underlying analysis method was adapted from (Olstad et al., 2019) and is based on the periodic changes of pixel intensities in the image caused by ciliary beating that are used by the plugin to determine ciliary beat frequency. The intensity time course at each pixel in the image was converted into a frequency spectrum using a Fast-

Fourier-Transformation (code: edu.emory.mathcs.jtransforms.fft by Piotr Wendykier, Emory University). Each spectrum was smoothed with a user-defined averaging sliding window (5 Hz). The position and power of the highest peak in the spectrum within a user-defined range was determined (will be referred as primary frequency). The user-defined range was defined as 3 to 62.5 Hz, which represents a quarter of the acquisition frequency (250 Hz). Next, a custom noise-threshold algorithm was applied to separate the image into noise and signal regions: (1) Pixels were sorted by the power of the primary frequency; (2) The average and standard deviation (SD) of the 20% of pixel with the lowest power were determined and used to define a power threshold as average + 1.5x SD; (3) all pixels with a primary frequency power above the threshold were considered as signal pixels, all other pixels were considered as noise pixels. A "noise" power spectrum was determined as the average + 1.5x SD of all power spectra from pixels belonging to noise regions. The "noise" power-spectrum was subtracted from the power spectrum at all "signal" pixel positions (power below zero was set to zero). For each cell, the resulting power spectrum from all "signal" pixels was averaged in to a "signal" power spectrum. The frequency of the highest peak in the "signal" power spectrum within the user-defined range of 3 to 62.5 Hz determined the ciliary beat frequency. All results were scrutinized by a trained observer.

Color-coded time projections of swimming mouse sperm

To generate color-coded time projections of time-lapse images of mouse sperm, images were processed as follows in FIJI (Schindelin et al., 2012). They were pre-processed using SpermQ_Preparator (Hansen et al., 2018): (i) pixel intensities were inverted; (ii) pixel intensities were rescaled so that intensities in the image covered the whole bit range; (iii) the image stack was blurred with a Gaussian blur (sigma = 0.5 px) to reduce noise; (iv) a median intensity projection of the image stack was subtracted from all images in the stack to remove

the static image background; (5) pixel intensities were again rescaled so that intensities in the image covered the whole bit range; (6) the background was subtracted using ImageJ's 'Subtract Background' method (radius 5 px). Next, a selected time span (time indicated in the figure legend) was converted into a color-coded time projection using FIJI's function 'Temporal-Color Code' (Schindelin et al., 2012).

QUANTIFICATION AND STATISTICAL ANALYSIS

Statistics

All statistical analysis was carried out using GraphPad Prism 8 (version 8.4.1; GraphPad software, USA) as described in the text. To determine statistical significance, unpaired *t*-tests were used to compare between two groups, unless otherwise indicated. The mean ± the standard error of the mean (SEM) is reported in the figures as indicated. Statistical significance was set at $P<0.05$. Fisher's exact test was used to determine the significance in animal studies and to classify ciliary bundles in motile or immotile during mTEC maturation. All *in vitro* experiments were repeated in three biological replicates and several litters were used for *in vivo* studies, as indicated in each section.

DATA AND CODE AVAILABILITY

The accession number for total RNA-seq data related to splicing analysis at Gene Expression Omnibus (GEO) is GSE157269GSE157269. Polysomal, monosomal and cytoplasmic RNA-sequencing data are available at

http://181.89.68.25:8080/94d277ffb060705f65f4fb94a1fbcf98/.

The mass spectrometry proteomics data are available at ProteomeXchange Consortium via the PRIDE partner repository with the dataset identifier PXD019859.

Username:reviewer79803@ebi.ac.uk; Password:4HAr4wOY. All custom MATLAB scripts and ImageJ plugins are available upon request.